AGU PUBLICATIONS

JGR

Journal of Geophysical Research: Planets

RESEARCH ARTICLE
10.1002/2013JE004559

Key Points:
- The uncertainty in the lunar Love number is improved by a factor of 5
- The moment of inertia of the solid Moon is improved by an order of magnitude
- Models fit a fluid outer and solid inner core plus low Q in the lower mantle

Correspondence to:
J. G. Williams,
James.G.Williams@jpl.nasa.gov

Citation:
Williams, J. G., et al. (2014), Lunar interior properties from the GRAIL mission, *J. Geophys. Res. Planets*, *119*, doi:10.1002/2013JE004559.

Received 11 OCT 2013
Accepted 7 JUN 2014
Accepted article online 12 JUN 2014

Lunar interior properties from the GRAIL mission

James G. Williams[1], Alexander S. Konopliv[1], Dale H. Boggs[1], Ryan S. Park[1], Dah-Ning Yuan[1], Frank G. Lemoine[2], Sander Goossens[2,3], Erwan Mazarico[2], Francis Nimmo[4], Renee C. Weber[5], Sami W. Asmar[1], H. Jay Melosh[6], Gregory A. Neumann[2], Roger J. Phillips[7], David E. Smith[8], Sean C. Solomon[9,10], Michael M. Watkins[1], Mark A. Wieczorek[11], Jeffrey C. Andrews-Hanna[12], James W. Head[13], Walter S. Kiefer[14], Isamu Matsuyama[15], Patrick J. McGovern[14], G. Jeffrey Taylor[16], and Maria T. Zuber[8]

[1]Jet Propulsion Laboratory, California Institute of Technology, Pasadena, California, USA, [2]NASA Goddard Space Flight Center, Greenbelt, Maryland, USA, [3]Department of Physics, University of Maryland, Baltimore, Maryland, USA, [4]Department of Earth and Planetary Sciences, University of California, Santa Cruz, California, USA, [5]NASA Marshall Space Flight Center, Huntsville, Alabama, USA, [6]Department of Earth, Atmospheric, and Planetary Sciences, Purdue University, West Lafayette, Indiana, USA, [7]Planetary Science Directorate, Southwest Research Institute, Boulder, Colorado, USA, [8]Department of Earth, Atmospheric, and Planetary Sciences, Massachusetts Institute of Technology, Cambridge, Massachusetts, USA, [9]Lamont-Doherty Earth Observatory, Columbia University, Palisades, New York, USA, [10]Department of Terrestrial Magnetism, Carnegie Institution of Washington, Washington, District of Columbia, USA, [11]Institut de Physique du Globe de Paris, Paris, France, [12]Department of Geophysics and Center for Space Resources, Colorado School of Mines, Golden, Colorado, USA, [13]Department of Geological Sciences, Brown University, Providence, Rhode Island, USA, [14]Lunar and Planetary Institute, Houston, Texas, USA, [15]Lunar and Planetary Laboratory, University of Arizona, Tucson, Arizona, USA, [16]Hawaii Institute of Geophysics and Planetology, University of Hawaii, Honolulu, Hawaii, USA

Abstract The Gravity Recovery and Interior Laboratory (GRAIL) mission has sampled lunar gravity with unprecedented accuracy and resolution. The lunar *GM*, the product of the gravitational constant *G* and the mass *M*, is very well determined. However, uncertainties in the mass and mean density, $3345.56 \pm 0.40\ \mathrm{kg/m^3}$, are limited by the accuracy of *G*. Values of the spherical harmonic degree-2 gravity coefficients J_2 and C_{22}, as well as the Love number k_2 describing lunar degree-2 elastic response to tidal forces, come from two independent analyses of the 3 month GRAIL Primary Mission data at the Jet Propulsion Laboratory and the Goddard Space Flight Center. The two k_2 determinations, with uncertainties of ~1%, differ by 1%; the average value is 0.02416 ± 0.00022 at a 1 month period with reference radius $R = 1738$ km. Lunar laser ranging (LLR) data analysis determines $(C - A)/B$ and $(B - A)/C$, where $A < B < C$ are the principal moments of inertia; the flattening of the fluid outer core; the dissipation at its solid boundaries; and the monthly tidal dissipation $Q = 37.5 \pm 4$. The moment of inertia computation combines the GRAIL-determined J_2 and C_{22} with LLR-derived $(C - A)/B$ and $(B - A)/C$. The normalized mean moment of inertia of the solid Moon is $I_s/MR^2 = 0.392728 \pm 0.000012$. Matching the density, moment, and Love number, calculated models have a fluid outer core with radius of 200–380 km, a solid inner core with radius of 0–280 km and mass fraction of 0–1%, and a deep mantle zone of low seismic shear velocity. The mass fraction of the combined inner and outer core is ≤1.5%.

1. Introduction

The lunar interior is hidden from direct inspection, so it must be investigated by measurements on and above the surface. Apollo seismic experiments showed that the Moon has a thin crust, a thick mantle, and an attenuating layer of low seismic velocities in the deep mantle [*Nakamura et al.*, 1973, 1974, 1976; *Nakamura*, 1983; *Toksöz et al.*, 1974; *Goins et al.*, 1981]. A dense inner core was expected but not detected. *Brett* [1973] argued that Fe-Ni-S phase relations allowed a fluid outer core with a lower freezing temperature than liquid Fe. Apollo-era and Lunar Prospector magnetic field measurements appeared to show a weak, long-lasting induced field from an electrically conductive core [*Goldstein et al.*, 1976; *Russell et al.*, 1981; *Hood et al.*, 1999; *Shimizu et al.*, 2013]. Remanent magnetism in lunar samples may result from an early lunar dynamo in a fluid core [*Garrick-Bethell et al.*, 2009; *Suavet et al.*, 2013]. A present-day fluid state for the outer core was identified by lunar laser ranging (LLR) determination of pole orientation, which provided evidence for dissipative torques at the boundary between the fluid core and the solid mantle [*Williams et al.*, 2001]. Recent reanalysis of Apollo seismic data has led two groups to propose core radii from the identification of reflections of seismic waves off a solid-fluid boundary [*Weber et al.*, 2011; *Garcia et al.*, 2011]. The former group also

presented radii for a solid inner core and a seismic low-velocity layer in the deep mantle. After 4 decades, knowledge of the deep lunar interior is still limited, and additional information is needed. Models of interior structure and properties must satisfy mean density, moment of inertia, and Love numbers, which are among the subjects of this paper. The mean density and moment of inertia constrain the dependence of density on depth. The tidal response, expressed as Love numbers, constrains the profile of elastic properties. Tidal energy dissipation is another key lunar property of the lunar interior that influences the frequency dependence of Love numbers and governs orbital evolution and the generation of deep moonquakes.

Analyses of radio tracking of lunar-orbiting spacecraft and laser ranging to surface retroreflectors provide information for computing the lunar moment of inertia. Both techniques use Love numbers to characterize tidal response. Lunar laser ranging also determines phase-shifted tides arising from tidal dissipation. This paper presents current knowledge of density, moments of inertia, Love numbers, and dissipation parameters. NASA's Gravity Recovery and Interior Laboratory (GRAIL) mission [*Zuber et al.*, 2013a], with very accurate satellite-satellite tracking [*Klipstein et al.*, 2013], has improved the static lunar gravity field by many orders of magnitude [*Konopliv et al.*, 2013; *Lemoine et al.*, 2013; *Zuber et al.*, 2013b]. Uncertainty in the determination of the spherical harmonic degree-2 tidal potential Love number k_2 is shown to improve several fold. Model calculations show that the Love number is sensitive to the fluid outer core and attenuating zone.

An overview of the mission has been presented by *Zuber et al.* [2013a]. The GRAIL mission design was discussed by *Roncoli and Fujii* [2010], and the recovery of the gravity field, tidal response, and core information from the satellite-satellite-tracking data was simulated by *Park et al.* [2012]. A complete description of the GRAIL system as well as science data quality was given by *Asmar et al.* [2013]. Several papers are based on the Primary Mission (PM) data from 1 March to 29 May in 2012. *Zuber et al.* [2013b] presented an overview of the high-resolution gravity field from the Primary Mission. *Wieczorek et al.* [2013] determined the upper crustal density and constrained the average crustal thickness. *Andrews-Hanna et al.* [2013] found linear gravity features that appear to be from ancient dikes. Numerical models for the origin of lunar mascon basins consistent with GRAIL measurements were investigated by *Melosh et al.* [2013]. This paper on the lunar interior uses results from two companion GRAIL data analysis papers [*Konopliv et al.*, 2013; *Lemoine et al.*, 2013] that also incorporate Primary Mission data.

This paper explores the mean moment and potential Love number determined from the GRAIL data analysis. In section 2, the lunar mass and mean density are derived from the GRAIL and ephemeris *GM* values, the product of the gravitational constant *G* and the lunar mass *M*, combined with mean radius determinations from altimetry missions. The moment of inertia of the solid Moon, the combined crust, mantle, and any inner core (see section 4) follows from the GRAIL-determined degree-2 gravity coefficients, Love number, and lunar laser ranging determinations of variations in three-dimensional lunar orientation called physical librations. Section 3 reviews that theory, section 4 discusses the tide and physical libration models, and section 5 gives the moment and Love number determinations. In section 6, the LLR dissipation solution is updated, since it is relevant to interior models. Model calculations give insight into interior structure. Model computations match the mean density, moment of inertia, and Love number determinations in section 7. Section 8 extends the monthly Love numbers to other periods. Finally, future possibilities are discussed in section 9, and a summary is given in section 10.

2. Mass and Density

Basic properties of the whole Moon include mass and mean radius, from which the mean density is derived. The determination of the orbit period and semimajor axis of lunar-orbiting spacecraft provides lunar *GM*, the product of the gravitational constant *G* and the mass *M*, from analysis of radio-tracking data [*Konopliv et al.*, 1998; *Matsumoto et al.*, 2010; *Goossens et al.*, 2011b]. The analysis of radio-tracking data from Earth to spacecraft orbiting Mars, Venus, and other planets is also sensitive to lunar *GM*, since the center of the Earth is displaced from the Earth-Moon center of mass, and the displacement reflects the orbital motion of the Moon.

Several determinations of lunar *GM* from the analyses of lunar-orbiting spacecraft-tracking data are given in Table 1. The Lunar Prospector (LP) fields include tracking data from the five Lunar Orbiter (LO) spacecraft, the Apollo 15 and 16 subsatellites, and the Clementine and Lunar Prospector (LP) missions [*Konopliv et al.*, 2001]. The Selenological and Engineering Explorer Gravity Model (SGM) fields added tracking data from the Small Missions for Advanced Research in Technology 1 mission and the Selenological and Engineering Explorer (SELENE) mission, including the main spacecraft and the two subsatellites [*Matsumoto et al.*, 2010]. In addition

Table 1. Recent Lunar *GM* Determinations

ID	*GM* in km^3/s^2	Data Sets[a]	Citation
LP75G	4902.8003 ± 0.0012	LO to LP tracking	*Konopliv et al.* [1998]
LP150Q	4902.80108 ± 0.0008	LO to LP tracking	*Konopliv* [2000]
DE421	4902.80008 ± 0.00010	Interplanetary range + LLR through 2007	*Folkner et al.* [2008]; *Williams et al.* [2008]
-	4902.8002 ± 0.002	LO to LP tracking	*Goossens and Matsumoto* [2008]
SGM100h	4902.80212 ± 0.0026	LO to SELENE tracking	*Matsumoto et al.* [2010]
SGM100i	4902.80080 ± 0.0018	LO to SELENE tracking + SELENE VLBI	*Goossens et al.* [2011a]
SGM150j	4902.79918 ± 0.0017	LO to SELENE tracking + VLBI + LP XM	*Goossens et al.* [2011b]
GL0660B	4902.80031 ± 0.00044	Dual spacecraft tracking	*Konopliv et al.* [2013]
GRGM 660PRIM	4902.79981 ± 0.00019	Dual spacecraft tracking	*Lemoine et al.* [2013]
DE430	4902.80007 ± 0.00014	Interplanetary range + LLR through 2012	This paper

[a]LO = Lunar Orbiter, LP = Lunar Prospector, and XM = Extended Mission.

to radio tracking from the ground, SELENE mission tracking between satellites allowed extensive farside tracking for the first time. SELENE's very long baseline interferometry (VLBI) data were added for later fields [*Goossens et al.*, 2011a, 2011b]. The uncertainties in the table are larger than the formal uncertainties, typically 10 times the formal uncertainties for the Moon-orbiting determinations, but a factor of 20 is used for the first two SGM results.

Recent lunar *GM* values from the Jet Propulsion Laboratory (JPL) ephemerides DE421 [*Folkner et al.*, 2008; *Williams et al.*, 2008] and DE430 [*Williams et al.*, 2013; *Folkner et al.*, 2014] are given in Table 1. These values resulted from analyses of interplanetary tracking of spacecraft from Earth. Both ephemerides were generated from the joint analyses of LLR data and interplanetary radio range, astrometric angle, and spacecraft VLBI data. In combination with the LLR-determined *GM* of Earth + Moon, tracking of planetary-orbiting and landed spacecraft gives the Earth/Moon mass ratio and hence the lunar *GM* from the motion of the center of the Earth with respect to the Earth-Moon center of mass. Ephemeris DE421 also processed tracking data from the Near-Earth Asteroid Rendezvous spacecraft orbiting 433 Eros. Ephemeris DE430 processed 5 more years of planetary-tracking data than DE421, but it did not use the Eros data. The DE421 and DE430 *GM* values are in good agreement, but the latter has a larger uncertainty, perhaps due to a more conservative error estimate or because of the lack of Eros data.

GRAIL analyses (gravity fields GL0660B and GRGM660PRIM) improve the lunar-orbiting spacecraft values of *GM* in Table 1, but the ephemeris values from joint LLR and interplanetary solutions (DE421 and DE430) are more accurate. The *GM* accuracies are approaching levels at which there are relativity effects that depend on the coordinate frame implemented for the dynamical calculations. The tabulated values are from JPL and Goddard Space Flight Center (GSFC) programs that employ a solar system barycentric frame. The unweighted average of the two GRAIL *GM* values is 4902.80006 km^3/s^2, compatible with the LLR and planetary DE430 ephemeris value of 4902.80007 ± 0.00014 km^3/s^2. In a relative sense, all of the *GM* determinations of Table 1 are much more accurate than the uncertainty in the gravitational constant *G*. Dividing *GM* by the Committee on Data for Science and Technology 2010 value of $G = (6.67384 \pm 0.00080) \times 10^{-11}$ $m^3/kg\,s^2$ [*Mohr et al.*, 2012] gives the lunar mass

$$M = (7.34630 \pm 0.00088) \times 10^{22}\ \text{kg}. \quad (1)$$

The uncertainty in the mass is dominated by the 0.012% uncertainty in *G*.

Table 2. Recent Lunar Mean Radii Determined From Laser Altimetry

Mission	Identification	R_m in km	Citation
Clementine	GLTM 2	1737.103 ± 0.015	*Smith et al.* [1997]
Chang'E-1	CLTM-s01	1737.013	*Ping et al.* [2009]
SELENE	STM359_grid-02	1737.15 ± 0.01	*Araki et al.* [2009]
LRO		1737.153 ± 0.010	*Smith et al.* [2010]
LRO	LRO_LTM01_PA	1737.1512	*Neumann* [2013]

Downward pointing lasers have performed global lunar altimetry on the Clementine, Chang'E-1, SELENE, and Lunar Reconnaissance Orbiter (LRO) missions. Table 2 summarizes the results for the mean lunar radius from the four missions. *Fok et al.* [2011]

found that a bias of 150 m needs to be added to the Change'E-1 radii. The last entry in the table is the most accurate, with a mean radius $R_m = 1737.1512$ km and an uncertainty <1 m. The SELENE result is compatible and so is the Change'E-1 result after applying the *Fok et al.*'s correction. The earlier Goddard Lunar Topography Model 2 (GLTM 2) radius [*Smith et al.*, 1997] is only 50 m less. We adopt $R_m = 1737.151$ km for the mean lunar radius. With the above mass, the mean density is

$$\rho_m = 3345.56 \pm 0.40\ \mathrm{kg/m^3}, \tag{2}$$

and the uncertainty in the density is limited by the 0.012% uncertainty in G and mass. This mean density is similar to the likely density of lunar mantle material, so any much denser core material must be a small fraction of the total.

GRAIL improves the orbiting spacecraft GM values of the Moon, but the lunar and planetary value of $4902.80007 \pm 0.00014\ \mathrm{km^3/s^2}$ appears to be more accurate. The uncertainty in G controls the uncertainty for the mass and the mean density $\rho_m = 3345.56 \pm 0.40\ \mathrm{kg/m^3}$.

3. Moment of Inertia Theory

An important property of the Moon is its moment of inertia. The three principal moments of inertia of the whole Moon around three orthogonal principal axes are ordered $A < B < C$. The principal axis z near the axis of rotation is associated with moment C, and the principal axis x associated with moment A points near the mean Earth direction. The principal axis y is associated with moment B. The moment of inertia values result from combining the data analysis results from two techniques: the degree-2 gravity field from orbiting spacecraft and physical libration parameters from LLR. The combination of the LLR and spacecraft results gives the normalized moments A/MR^2, B/MR^2, and C/MR^2 and the mean moment $I_m/MR^2 = (A+B+C)/3MR^2$, where M is the mass of the Moon and R is the reference radius for gravity. This paper combines the gravity and lunar laser ranging results.

The unnormalized second-degree gravity coefficients are related to the moment differences through their definitions.

$$J_2 = \frac{2C - (A+B)}{2MR^2} \tag{3}$$

$$C_{22} = \frac{B-A}{4MR^2}. \tag{4}$$

Because we are using the principal axes to define the coordinate frame, the static values of $C_{21} = S_{21} = S_{22} = 0$.

The lunar physical librations, the time-variable three-axis rotation or lunar orientation, are sensitive to the relative moment differences. For the entire Moon, these are

$$\alpha = \frac{C-B}{A} \tag{5}$$

$$\beta = \frac{C-A}{B} \tag{6}$$

$$\gamma = \frac{B-A}{C}. \tag{7}$$

Two of these three parameters are independent. The relation among them is

$$\alpha - \beta + \gamma = \alpha\beta\gamma. \tag{8}$$

Using the above definitions for J_2, C_{22}, β, and γ, the normalized polar moment C/MR^2 comes from two expressions.

$$\frac{C}{MR^2} = \frac{4C_{22}}{\gamma} \tag{9}$$

$$\frac{C}{MR^2} = \frac{2J_2(1+\beta)}{2\beta - \gamma + \beta\gamma}. \tag{10}$$

Which expression is more accurate depends on the accuracies of J_2, C_{22}, β, and γ. With a C/MR^2 value, the other two moments are given by

$$\frac{A}{MR^2} = \frac{(1-\beta\gamma)}{(1+\beta)}\frac{C}{MR^2} \tag{11}$$

$$\frac{B}{MR^2} = \frac{(1+\gamma)}{(1+\beta)}\frac{C}{MR^2}. \tag{12}$$

So β and γ along with either J_2 or C_{22} can give all three moments. A version of these expressions appeared in *Williams et al.* [1973] and *Ferrari et al.* [1980]. *Williams et al.* [2001] gave some expressions, and *Bills* [1995] presented all major combinations. An expression for B/MR^2 involving J_2, C_{22}, and β follows

$$\frac{B}{MR^2} = \frac{J_2 + 2C_{22}}{\beta}. \tag{13}$$

Using two or three measured parameters, the expressions above give three ways to obtain B/MR^2 and two ways to obtain both C/MR^2 and A/MR^2. *Bills* [1995] presented other expressions and showed that it is always possible to write the three principal moments using two or three parameters. It is always necessary to combine physical libration and gravity field parameters.

The mean moment is $I_m = (A+B+C)/3$. With the three principal moments and β and γ

$$\frac{I_m}{MR^2} = \frac{(3+\beta+\gamma-\beta\gamma)}{3(1+\beta)}\frac{C}{MR^2} \tag{14}$$

$$\frac{I_m}{MR^2} = \frac{(3+\beta+\gamma-\beta\gamma)}{3(1+\gamma)}\frac{B}{MR^2} \tag{15}$$

$$\frac{I_m}{MR^2} = \frac{(3+\beta+\gamma-\beta\gamma)}{3(1-\beta\gamma)}\frac{A}{MR^2}. \tag{16}$$

Bills [1995] showed that the mean moment can be calculated from any three of the four parameters: J_2, C_{22}, β, and γ.

To determine the moments of inertia, it is necessary to combine physical libration and gravity field parameters. There are three principal moments and four input quantities, but only three input parameters are needed. With two parameters from GRAIL and two from LLR, we will compute and compare three estimates for each mean moment in section 5. Some combinations are more accurate than others, since some input parameters are better known than others. Before GRAIL, the three parameters that gave the highest accuracy for moments were J_2, β, and γ (Appendix). With GRAIL results, moments from J_2, C_{22}, and β and J_2, β, and γ are the most accurate. Moments from C_{22}, β, and γ are less accurate but useful as a check. The combination J_2, C_{22}, and γ has nearly the same information content as C_{22}, β, and γ, because the first-order part of both is $4C_{22}/\gamma$.

4. Tide and Physical Libration Models

The expressions of the previous section are appropriate for the whole Moon. This section considers the consequences of both tides and a core structure that involves a liquid outer core and a solid inner core. The physical librations are the time-varying three-dimensional lunar orientation: the direction of the pole and the rotation about that pole. The spacecraft analysis programs read physical libration and ephemeris files. These files are generated by integrations using parameters obtained from joint LLR and planetary solutions. The physical libration model in the LLR software is discussed in this section.

The tidal Love numbers characterize the elastic response of the Moon to an imposed tidal potential. The degree-2 potential Love number is k_2, and the displacement Love numbers are h_2 for the vertical and l_2 for the horizontal. Tracking of lunar-orbiting satellites is sensitive to k_2 through perturbations to their orbits. The physical librations are also affected by k_2, which gives LLR sensitivity to this Love number as well. In addition, LLR has sensitivity to the tidal displacements of the surface sites.

The second-degree tide-raising potential from body p (Earth or Sun) at a radius r from the center of the Moon is

$$V_{2p}(r,\theta) = \frac{GM_p r^2}{2r_p^3}\left(3\cos^2\theta - 1\right), \tag{17}$$

where G is the gravitational constant, M_p is the mass of tide-raising body p, θ is the Moon-centered angle between the body p and the point selected for the potential, r_p is the distance to body p, and $r < r_p$. For r equal to a reference radius R, the simplest form for the potential from the tidal response of a spherical body is $V_{2pt}(R,\theta) = k_2\, V_{2p}(R,\theta)$.

$$V_{2pt}(R,\theta) = \frac{k_2 G M_p R^2}{2r_p^3}\left(3\cos^2\theta - 1\right). \tag{18}$$

For the potentials here, excess mass gives a positive potential and stronger attraction, which is a common sign convention in geodesy and astronomy. For a point at a radius $r \geq R$, the potential from the tidal response is

$$V_{2pt}(r,\theta) = \frac{k_2 G M_p R^5}{2r_p^3 r^3}\left(3\cos^2\theta - 1\right). \tag{19}$$

Now θ is the Moon-centered angle between the tide-raising body p and an external point at radius r. The gradient of equation (19) provides accelerations. Less simple tidal forms could introduce multiple k_{2m}, where m is the order of the second-degree response [*Konopliv et al.*, 2013; *Lemoine et al.*, 2013], phase shifts or time delays due to dissipation (section 6), frequency-dependent k_2 (section 8) [*Efroimsky*, 2012a, 2012b; *Nimmo et al.*, 2012], a Moon with nonspherical properties [*Zhong et al.*, 2012], or trigonometric series representations. There are also third- and higher-degree tides, which do not modify the moments of inertia; these higher-degree tides weaken by 2 orders of magnitude per degree.

The tidal potential, expressed by equations (18) and (19), results from distortions that contribute variable and constant parts to the moment of inertia matrix. Cos θ is the dot product between two unit vectors. One unit vector, $\mathbf{u} = \mathbf{r}_p/r_p$, with three components u_i, is directed from the center of the Moon toward the center of the tide-raising body p (Earth or Sun). The other unit vector, $\mathbf{r}/r$, points from the center of the Moon toward the location selected for the potential. The elastic tidal distortions of the moment of inertia matrix elements depend on $\mathbf{u}(t)$ and $r_p(t)$, which are functions of time.

$$I_{tij} = \frac{k_2 M_p R^5}{r_p^3}\left(u_i u_j - \frac{\delta_{ij}}{3}\right). \tag{20}$$

Parameter δ_{ij} is the Kronecker delta function. There are small variations in all the three components of $\mathbf{u}$ that depend on lunar orbit and orientation. For a coordinate frame rotating with the Moon, optical librations reach about 0.1 radian and the average u_1 component of the Earth is $<u_1> = <(1 - u_2^2 - u_3^2)^{1/2}> \approx 1 - <u_2^2>/2 - <u_3^2>/2 = 0.9934$, where $<>$ denotes a time average. The three diagonal elements of the moment matrix have large constant parts from $u_1 u_1$ and δ_{ii}, and all of the nine elements of this symmetrical matrix have smaller variable parts. The sum of the diagonal elements is 0, so the mean moment does not have tidal variations. The distortions of the Moon due to solar tides are 2 orders of magnitude smaller than the distortions due to the Earth. Both *Bills* [1995] and *Williams et al.* [2001] considered the effect of tidal distortion. The latter authors also considered spin distortion, which has very small variations. For more about the lunar and planetary integrator formulation, see *Standish and Williams* [2012] and *Folkner et al.* [2014].

The tidal distortion of the moment of inertia matrix is related to the tidal variations of the degree-2 gravity field coefficients. The unnormalized tidal variations ΔJ_2 and ΔC_{22} come from the definitions (3) and (4):

$$\Delta J_2 = \frac{2I_{t33} - (I_{t11} + I_{t22})}{2MR^2} \tag{21}$$

$$\Delta C_{22} = \frac{I_{t22} - I_{t11}}{4MR^2}. \tag{22}$$

The three remaining degree-2 coefficients have tidal variations

$$\Delta C_{21} = -\frac{I_{t13}}{MR^2} \tag{23}$$

$$\Delta S_{21} = -\frac{I_{t23}}{MR^2} \tag{24}$$

$$\Delta S_{22} = -\frac{I_{t12}}{2MR^2}. \tag{25}$$

These time-varying alterations of the degree-2 gravity coefficients are used in the lunar and planetary integrator [*Standish and Williams*, 2012; *Folkner et al.*, 2014]. The expressions used for the spacecraft analysis [*Konopliv et al.*, 2013; *Lemoine et al.*, 2013] are equivalent to equations (20)–(25). Tidal displacements of the retroreflectors in the LLR software use the potential (equation (17)) factored by h_2/g and its derivative factored by l_2/g, where g is the surface gravitational acceleration.

Following section 3 of *Williams et al.* [2001], the tide and spin distortions contribute to the moment of inertia matrix

$$\mathbf{I}(t) = \mathbf{I}_{tr} + \mathbf{I}_{pt} + \mathbf{I}_{vt}(t) + \mathbf{I}_{vs}(t), \tag{26}$$

where *tr* stands for tide removed and the $\mathbf{I}_{tr}$ matrix is constant with diagonal elements A, B, and C; subscript *pt* is the permanent tide, *vt* is the variable tide, and *vs* is from the variable spin distortion. The spin-distorted $\mathbf{I}_{vs}$ in the lunar integration of orbit and physical librations is formulated to null out the mean diagonal elements, as explained by *Williams et al.* [2001]. The matrix $\mathbf{I}_t(t) = \mathbf{I}_{pt} + \mathbf{I}_{vt}(t)$, where $\mathbf{I}_t(t)$ from equation (20) is separated into constant and variable parts in equation (26). The β and γ in the LLR software and the J_2 and C_{22} in the JPL and GSFC spacecraft analysis programs correspond to the constant diagonal part of the $\mathbf{I}_{tr}$ matrix. In the nomenclature used for Earth zonal coefficients, the tide-removed part is "tide free" and the tide-removed plus permanent-tide parts correspond to the "zero tide." In the spacecraft and LLR software, the tide matrices $\mathbf{I}_{pt}$ and $\mathbf{I}_{vt}$ and spin matrix $\mathbf{I}_{vs}$ are proportional to the potential Love number k_2 that describes the tidal response of the Moon. Matrix $\mathbf{I}_{tr}$ is diagonal, but $\mathbf{I}_{pt}$, $\mathbf{I}_{vt}$, and $\mathbf{I}_{vs}$ have off diagonal as well as diagonal elements. The variable part from spin is 3 orders of magnitude smaller than the variable part from tides and can be ignored in many applications.

As described by *Williams et al.* [2001], the $\mathbf{I}_{tr}$ matrix was referred to as "rigid" rather than "tide removed." It could also be called long term. Our objective here is to obtain a formulation that works for a year for GRAIL and for decades for other lunar missions and LLR. The long-term past relaxation of the Moon's figure and its connection to orbital and thermal evolution are important questions [*Matsuyama*, 2013], but we do not pursue them here. Note that the Moon's shape is not near an equilibrium shape for the current Earth distance, in contrast to a common first approximation for rapidly spinning planets and for large icy satellites.

The simple form of the tidal potential (equation (19)) is equivalent to the permanent (*pt*) and variable (*vt*) parts of the moment matrices in equation (26). These matrices are proportional to the k_2 value used with the potential; Table 5 in *Williams et al.* [2001] gives the six elements of $\mathbf{I}_{pt}/k_2$ that may be multiplied by a value of k_2. The constant parts of the off-diagonal 1,2 and 1,3 elements are 3 orders of magnitude smaller than the diagonal terms. These small off-diagonal constant terms arise, because the principal axes are not quite aligned with the mean direction to the Earth and the mean axis of rotation owing to torques from third- and higher-degree gravity field coefficients [*Eckhardt*, 1973; *Kaula and Baxa*, 1973]. The permanent tide parts of $\Delta J_2/k_2$ and $\Delta C_{22}/k_2$ come from the diagonal tidal elements and are also given in the cited Table 5; they follow from the definitions (3) and (4) leading to equations (21) and (22). The permanent tide parts of β and γ would come from their definitions (6) and (7) but are not given in that table.

A matrix of interest to measurements using spacecraft or LLR is the permanent moment matrix $\mathbf{I}_p = \mathbf{I}_{tr} + \mathbf{I}_{pt}$, where permanent refers to decades rather than aeons. During solutions, the variable tidal matrix $\mathbf{I}_{vt}$ should be distinct from the constant $\mathbf{I}_p$ if the data sample the variations well. There is a 6 year beat between the largest tidal terms: the 27.555 day anomalistic period of ΔJ_2, ΔC_{22}, and ΔS_{22} and the 27.212 day argument-of-latitude period of ΔC_{21}. The LLR data set is 4 decades long, so the separation of these and other periods should be good. The GRAIL Primary Mission was only 3 months long, and the tidal periods longer than a month are not as well sampled, but there is good sampling of the five spatial components. GRAIL's polar orbit passes over any lunar longitude at half-month intervals, which tends to obscure semimonthly tides away from the poles.

In the physical libration model, the Moon consists of a solid crust and mantle plus a uniform fluid core, but no solid inner core. Then each of the moment matrices may be split into solid and fluid parts. For the model, $A = A_s + A_f$, $B = B_s + B_f$, and $C = C_s + C_f$, where the subscript s indicates the solid mantle plus crust and subscript f stands for the fluid core. In reality, the principal moments of the fluid core may not be aligned with the mantle principal moments, but the moment ratio C_f/C is probably less than 10^{-3}, and the flattening of the outer core is small (see section 5 and Table 3), so the moment differences for the fluid core are small. The LLR

Table 3. Selected Lunar Parameters From the GRAIL-Compatible DE430 Solution

Parameter	DE430 Values[a]
β	$(631.0213 \pm 0.0031) \times 10^{-6}$
γ	$(227.7317 \pm 0.0042) \times 10^{-6}$
J_2	203.21568×10^{-6}
k_2	0.024059
h_2	0.048 ± 0.006
l_2	0.0107
C_f/C	7×10^{-4}
K/C	$(1.64 \pm 0.17) \times 10^{-8}$/d
f	$(2.46 \pm 1.4) \times 10^{-4}$
$[C_f - (A_f + B_f)/2]/C$	$(1.73 \pm 0.5) \times 10^{-7}$

[a]Solution parameters have uncertainties, except $[C_f - (A_f + B_f)/2]/C = f\, C_f/C$ is derived. Fixed parameters lack uncertainties: J_2 and k_2 are GRAIL-derived values, l_2 is a model value, and C_f/C is a nominal choice.

retroreflectors on the lunar surface are sensitive to the motion of the solid mantle + crust. The vector Euler equation for the solid Moon takes the form

$$\frac{d(\mathbf{I}_s\boldsymbol{\omega})}{dt} + \boldsymbol{\omega} x (\mathbf{I}_s\boldsymbol{\omega}) = \mathbf{T}, \tag{27}$$

where $\mathbf{I}_s$ is the moment of inertia matrix for the solid Moon, $\boldsymbol{\omega}$ is the solid Moon vector angular rate, the product $\mathbf{I}_s\boldsymbol{\omega}$ is the solid Moon angular momentum vector, and $\mathbf{T}$ is the torque vector. The external gravitational torques on the solid mantle depend on the whole-Moon $(C - A)$ and $(B - A)$, under the assumption of a uniform density fluid core. The shape of the core-mantle boundary (CMB) moves with the orientation of the mantle, affecting the potential and torque that arise from the density change at the CMB. By contrast, reorienting a uniform fluid does not change the potential, so the gravitational torques on the fluid are 0. There is an analogous equation to equation (27) for the fluid, but the torques arise from boundary interactions between the fluid core and the solid mantle. Those torques at the CMB act on both fluid core and solid mantle, but with opposite signs. The fluid interactions are very weak compared with the torques from gravity [*Goldreich*, 1967]. In the model, solid moments vary due to tides and spin, whereas fluid moments are constant. The physical libration response of the mantle depends on the moments of the solid layers through the product $\mathbf{I}_s\, d\boldsymbol{\omega}/dt$ in the Euler equations, so the physical librations depend on ratios $(C - A)/B_s$ and $(B - A)/C_s$. The LLR model that is used to fit range data includes whole-Moon β, γ, and J_2 plus a parameter for the ratio of the fluid core moment to the whole-Moon moment C_f/C. Currently, LLR data analysis does not obtain a significant solution for the ratio C_f/C. It does detect a flattening of the outer core. Nevertheless, the $(C - A)/B_s$ and $(B - A)/C_s$ values can be recovered from the β and γ solution parameters, even when the fluid moment ratio is not fit, so that those two values are expected to be well determined. In combination with spacecraft-determined J_2 and C_{22}, the normalized moments of the solid Moon A_s/MR^2, B_s/MR^2, C_s/MR^2, and the mean moment I_s/MR^2 can be determined.

Consider a lunar structure consisting of a solid crust and mantle plus a uniform fluid outer core and a solid inner core. *Goldreich* [1967] found that fluid interactions at the CMB are weak. Gravitational torques between a solid inner core and the mantle are expected to be much stronger than torques at the boundaries between a uniform fluid and adjacent solid structures. In the physical libration model, torques attributed to the CMB would, in a model with an inner core, be active at both fluid boundaries. In addition to fluid interactions, there would be torques on the inner core from the attraction of the Earth. The gravitational torques from Earth and mantle favor a synchronously rotating inner core. The fluid rotation is not synchronous [*Williams et al.*, 2001], and the fluid torques act against synchronous rotation of the inner core, but the influence of the fluid is very weak compared with the gravitational torques. Model calculations of gravitational torques by *Williams et al.* [2014] predict that the frequency of inner core free libration about a synchronous state is comparable to the mantle free libration frequency. The torques that control the inner core synchronous rotation are expected to be strong. In this paper we will assume that the orientation of any inner core is coupled strongly to the orientation of mantle plus crust by gravitational torques. In addition to synchronous rotation, the equator of the inner core should precess along the ecliptic plane with the same 18.6 year period as the mantle, but with a separate tilt to that plane [*Williams*, 2007]. From the combination of spacecraft-determined gravity field and LLR-determined physical libration information, we expect to obtain moments A_s/MR^2, B_s/MR^2, C_s/MR^2, and I_s/MR^2, where subscript s now indicates the solid mantle and crust plus the solid inner core.

The physical libration dynamical model incorporates elastic tides and rotation variations plus a fluid core. The physical librations of the mantle and crust are sensitive to $(C - A)/B_s$ and $(B - A)/C_s$. Consequently, the combination with spacecraft J_2 and C_{22} gives accurate solid Moon moments of inertia.

5. Moment of Inertia Results

This section combines the spacecraft-determined J_2 and C_{22} values with the LLR-determined β and γ to derive the model-dependent whole-Moon principal moments of inertia A, B, and C. Then we subtract off the LLR

model's fluid core moments A_f, B_f, and C_f to obtain the solid Moon moments A_s, B_s, and C_s, respectively. Several evaluations of the mean moment I_s are generated.

The spacecraft-determined J_2 and C_{22} and the LLR-determined β and γ are values pertinent to the tide-removed part $\mathbf{I}_{tr}$ of the moment matrix. If $\mathbf{I}(t)$ is well sampled in time by the data, its mean matrix value should be close to the permanent $\mathbf{I}_p = \mathbf{I}_{tr} + \mathbf{I}_{pt}$. The matrix $\mathbf{I}_{pt}/k_2$ given by *Williams et al.* [2001] must be multiplied by the k_2 of the solution. Since $\mathbf{I}_p$, the mean value of $\mathbf{I}(t)$, is closer to the measurements than $\mathbf{I}_{tr}$, we expect the "permanent" quantities of J_2, C_{22}, β, and γ to have smaller uncertainties than the tide-removed solution values after accounting for the uncertainty in and correlations with k_2.

To recover the moments of the solid Moon, the fluid A_f, B_f, and C_f need to be subtracted from the diagonal elements of $\mathbf{I}_{tr}$ and consequently from $\mathbf{I}_p = \mathbf{I}_{tr} + \mathbf{I}_{pt}$. The LLR integration program has a uniform fluid core density with no inner core interactions. Consequently, the CMB shape, with equatorial radii a_f and b_f and polar radius c_f, is related to the fluid moments, and $f = [C_f - (A_f + B_f)/2]/C_f \approx [(a_f + b_f)/2 - c_f]/c_f$, where the flattening parameter f is a small LLR solution parameter. The LLR model has $A_f = B_f$ or $a_f = b_f$, since little sensitivity of LLR to equatorial ellipticity is expected. The inner and outer radii of the fluid core and its moment ratio C_f/C are uncertain, but C_f/C is probably less than 10^{-3}. Past LLR physical libration integrations have been made with moment ratios 3×10^{-4} and 7×10^{-4} (see pre-GRAIL solutions in Table A1). The latter ratio is used here. Moment C_f is C times C_f/C, and $A_f = B_f = C_f\,(1 - f)$. The flattening f is a small correction when converting A and B to A_s and B_s.

To ensure high compatibility between the GRAIL and LLR results, a new integration of the lunar orbit and physical librations was made. This ephemeris is a combination of LLR and planetary data analysis. The new ephemeris is intended to replace DE421 [*Williams et al.*, 2008; *Folkner et al.*, 2008], JPL's standard lunar ephemeris since 2008, as the ephemeris recommended for lunar work. GRAIL data analysis supplied input values for Love number k_2 and a low-degree gravity field up to degree and order 6. These input values to the ephemeris integrations and fits are improved by adopting GRAIL results from the Primary Mission [*Konopliv et al.*, 2013; *Lemoine et al.*, 2013]. The full GRAIL field from the Primary Mission extended to degree and order 660, a precursor to GL0660B, but since LLR sensitivity to gravity coefficients drops off by 2 orders of magnitude per degree, a degree-6 field is more than adequate. Earth zonal gravity coefficients up to degree 5 have also been updated. The LLR solutions and integrations were iterated to ensure convergence. The final set of lunar and planetary orbits and lunar physical librations is called DE430. During the lunar integration, C_{22} is computed from J_2, β, and γ; it is not treated as an independent parameter in the LLR fits. Apart from J_2 and C_{22}, the other degree-2 coefficients are assumed to be 0, giving a principal axis frame for the tide-removed moment matrix.

LLR has been reviewed by *Dickey et al.* [1994] and *Murphy* [2013]. The LLR solution presented in Table 3 uses data from March 1970 to December 2012 totaling 18,548 ranges. The tabulated values and uncertainties were obtained while making solutions for the new ephemeris, DE430. During the fits, the displacement Love number l_2 was fixed at a model value of 0.0107, see Tables 6–8 in section 7. Three of the third-degree gravity coefficients were adjusted during the LLR fits: C_{32}, S_{32}, and C_{33}. This adjustment gives a better LLR fit, but the small differences from the GRAIL values are thought to indicate unmodeled effects in the physical libration model. The new ephemeris, DE430, is publicly available; lunar aspects have been documented by *Williams et al.* [2013], and equations of motion and planetary analysis have been described by *Folkner et al.* [2014]. The full set of parameters input to the lunar and planetary integration is included with the DE430 ephemeris files.

Pre-GRAIL LLR solutions for β and γ along with pre-GRAIL spacecraft solutions for J_2 and C_{22} are given in the Appendix. Two different fluid core moment ratios C_f/C are used for the LLR solutions to demonstrate the influence of that parameter. A comparison of Tables 3 and A1 shows that the LLR values for $\beta = (C - A)/B$ and $\gamma = (B - A)/C$ are improved by adopting the GRAIL low-degree gravity coefficients. There is an order of magnitude improvement in β.

In Table 3, the quantities with uncertainties were DE430 solution parameters or are derived from them. Parameters without uncertainties were fixed during the solution. The last four entries are parameters for a fluid core. The ratio C_f/C specifies the moment of inertia of the fluid outer core. It was a fixed input quantity, but the uncertainties on the last three parameters include a contribution from C_f/C uncertainty judged from Table A1 differences. The last entry is derived from the product $f\,C_f/C$. The parameter K/C in the physical libration model is a coefficient for dissipation from fluid motion at the CMB but more generally at both outer-core boundaries [*Williams et al.*, 2001]. This interaction first demonstrated that the outer core must be fluid. In

Table 4. Two Independent GRAIL Analysis Results for Unnormalized J_2 and C_{22} Gravity Coefficients, Degree-2 Love Numbers, and the Mean Solid Moment of Inertia Derived From Three Combinations With LLR-Derived β and γ

Parameter	GL0660B	GRGM660PRIM
R	1738.0 km	1738.0 km
k_{20}	0.02408 ± 0.00045	0.024165 ± 0.00228
k_{21}	0.02414 ± 0.00025	0.023915 ± 0.00033
k_{22}	0.02394 ± 0.00028	0.024852 ± 0.00042
k_2	0.02405 ± 0.000176	0.02427 ± 0.00026
k_{30}		0.00734 ± 0.00375
k_3	0.0089 ± 0.0021	
J_{2tr}	$(203.21572 \pm 0.00317) \times 10^{-6}$	$(203.22040 \pm 0.00855) \times 10^{-6}$
C_{22tr}	$(22.38184 \pm 0.00111) \times 10^{-6}$	$(22.38000 \pm 0.00079) \times 10^{-6}$
J_{2p}	$(203.30517 \pm 0.00070) \times 10^{-6}$	$(203.31028 \pm 0.00111) \times 10^{-6}$
C_{22p}	$(22.42635 \pm 0.00022) \times 10^{-6}$	$(22.42600 \pm 0.00014) \times 10^{-6}$
$J_{2p}, \beta, \gamma \rightarrow I_s/MR^2$	0.392733 ± 0.000003	0.392743 ± 0.000003
$C_{22p}, \beta, \gamma \rightarrow I_s/MR^2$	0.392715 ± 0.000008	0.392709 ± 0.000007
$J_{2p}, C_{22p}, \beta \rightarrow I_s/MR^2$	0.392730 ± 0.000002	0.392737 ± 0.000003

that paper the detection of K/C was a factor of 4 greater than its uncertainty. In Table 3 detection is nearly a factor of 10 greater than the uncertainty, so this indication of a fluid core is now very strong.

The second LLR indication of a fluid core in Table 3 comes from the core flattening in the model, $f = [C_f - (A_f + B_f)/2]/C_f$, the relative pole-to-equator moment difference. The physical libration model uses the moment difference definition, which is also a good approximation if there is a synchronous oblate inner core resulting in geometric flattening at both boundaries. For a uniform-density core, the product $f\,C_f/C = [C_f - (A_f + B_f)/2]/C$ is better determined than f. This latter quantity is a factor of 3 greater than its uncertainty, so evidence for the existence of the flattening is stronger than the value of the flattening itself. The pole-to-equator radius difference is on the order of 100 m. Note the similarity of the flattening in Table 3 to the theoretical value for a CMB in hydrostatic equilibrium with the existing nonhydrostatic mantle [*Meyer and Wisdom*, 2011]. In the Meyer and Wisdom study, the observed static degree-2 gravity field was assumed to arise in the lunar lithosphere. Extending the potential from the lithosphere downward, the flattening of the core-mantle interface was calculated by requiring the potential along its surface to be constant. Using a similar technique, *Le Bars et al.* [2011] obtained a theoretical CMB equatorial ellipticity of about 10^{-4}. By contrast, if the whole Moon were in hydrostatic equilibrium, the CMB flattening would be 2.2×10^{-5}, an order of magnitude smaller than the value determined for f, and the equatorial ellipticity would be 2.6×10^{-5}.

Two independent solutions for GRAIL-derived Love number k_2 and unnormalized J_2 and C_{22} are presented in Table 4: GL0660B from the JPL analysis group and software [*Konopliv et al.*, 2013] and GRGM660PRIM from the GSFC analysis and software [*Lemoine et al.*, 2013]. Data from the GRAIL Primary Mission were analyzed for each solution. Along with J_2, C_{22}, and the gravity field, the GRGM660PRIM solution included estimates of the three independent k_{20}, k_{21}, and k_{22} parameters, whereas the GL0660B solution constrained the three parameters to be equal, giving a single k_2. In Table 4, three unconstrained k_{2m} values are also given for the GL0660B column but from a separate related solution. The GRGM660PRIM column also gives a k_2 value that is the weighted combination of the three k_{2m} values (ignoring mutual correlations). The difference in the two independent determinations of the Love number k_2 is less than 1%. GRAIL analysis determines the Love number with an ~1% uncertainty, a factor of 5 improvement over pre-GRAIL knowledge (Appendix). The unweighted average of the two values and their uncertainties is 0.02416 ± 0.00022.

A comparison of the two solutions presented in Table 4, plus GM in Table 1 and C_{21}, S_{21}, and S_{22} [*Konopliv et al.*, 2013; *Lemoine et al.*, 2013], shows that there are differences in both parameter values and uncertainties. The difference in uncertainties reflects the sensitivity of such estimates to the choice of variables, analysis procedure, and data weighting. The comparison of the differences between the two sets of solution parameters with their uncertainties indicates that the J_{2p} values stand out with difference/uncertainty ratios of 7.3 and 4.6. For the other parameters, the largest ratio is 2.6. For J_2, it is only the permanent value that stands out. The much larger uncertainty on the tide-removed values is compatible with its difference. Accounting for the correlations with Love numbers, the transformation of J_2 and C_{22} from tide-removed to

permanent values reduced the calculated uncertainties as expected, but whereas the transformation decreased the C_{22} difference between the two solutions, the J_2 difference increased.

Expressions (11)-(16) are used to combine the J_2 and C_{22} gravity coefficients (Table 4) with the LLR-determined β and γ (Table 3) to derive the values of the solid mean moment of inertia I_s/MR^2 given in Table 4. The three most distinct combinations are presented: J_{2p}, β, and γ; then C_{22p}, β, and γ; and finally J_{2p}, C_{22p}, and β. The unweighted average of the three GL0660B estimates is 0.392726 with an RMS scatter of 7 in the last digit. The weighted average is 0.392730. The unweighted average of the three GRGM660PRIM values is 0.392730 with an RMS scatter of 15 in the last two digits. Mean moment values using the GRGM660PRIM J_{2p} value are largest. The weighted average is 0.392738. The unweighted average of all the six determinations is 0.392728 with a scatter of 12 in the last two digits. We give $I_s/MR^2 = 0.392728 \pm 0.000012$ as the GRAIL estimate of the mean moment of the solid Moon. Then $A_s/MR^2 = 0.392615$, $B_s/MR^2 = 0.392705$, and $C_s/MR^2 = 0.392863$, all with the same uncertainty. The moment differences are known with smaller uncertainty: $(C_s - A_s)/MR^2 = 2.4809 \times 10^{-4}$, $(C_s - B_s)/MR^2 = 1.5838 \times 10^{-4}$, $(B_s - A_s)/MR^2 = 0.8971 \times 10^{-4}$, $(C_s - I_s)/MR^2 = 1.3549 \times 10^{-4}$, $(B_s - I_s)/MR^2 = -0.2289 \times 10^{-4}$, and $(A_s - I_s)/MR^2 = -1.1260 \times 10^{-4}$.

In the Appendix, three recent pre-GRAIL spacecraft solutions are used for the degree-2 gravity coefficients. The comparison of Tables 4 and A2 shows that GRAIL J_2 and C_{22} have improved by an order of magnitude or more compared with pre-GRAIL values. For the mean moment of inertia of the solid Moon, I_s/MR^2, the GRAIL result is also improved by an order of magnitude over older results.

The results in Table 4 are for $R = 1738$ km, the standard reference radius for lunar gravity work. As a result of altimetry (see Table 2), the mean radius of the Moon is known to be 1737.151 km. How does one convert these values to different reference radii? Invariant degree-2 products in the potential are GMJ_2R^2 and $GMC_{22}R^2$ for constant coefficients. Table 1 in section 2 shows that the relative GM uncertainty is less than 10^{-7}, so just consider products J_2R^2 and $C_{22}R^2$. To convert J_2 and C_{22} from the 1738 km gravity standard to the topographic 1737.151 km radius, multiply by $(1738/1737.151)^2 = 1.000978$. Higher-degree coefficients involve higher powers of the radii, e.g., the product J_nR^n for degree n. From definitions (6) and (7), β and γ do not depend on the reference radius. Equations (9) through (16) show that the moments of inertia normalized by MR^2 depend on R^2. Consequently, the mean moment of inertia of the solid Moon depends on R^4. The Table 4 normalized mean solid moment I_s/MR^2 of 0.392728 ± 0.000012 converts to 0.393112 ± 0.000012 with the topographic radius. A uniform density sphere has a normalized mean moment of 0.4; a smaller value indicates that density increases inward.

For degree-2 tides, equation (19) gives the combination $GM_pk_2R^5/a_p^3$, where p stands for Earth or Sun. The relative uncertainty of GM_E is 10^{-9} [*Ries et al.*, 1992; *Ries*, 2007; *Dunn et al.*, 1999], whereas the GM_S uncertainty is on the order of 10^{-11} [*Williams et al.*, 2013]. The relative uncertainty of lunar semimajor axis a is 10^{-9}, and the length of the *AU* was known to better than 10^{-11} prior to recently becoming a defined quantity, so small differences in GM_E/a^3 or GM_S/AU^3 can be ignored compared with the radius R difference. To convert k_2 to the topographic radius, multiply by $(1738/1737.151)^5 = 1.002446$. For higher-degree Love numbers, consider the product k_nR^{2n+1} to be invariant. The averaged GRAIL Love number k_2 converts from 0.02416 ± 0.00022 to 0.02422 ± 0.00022, when R changes from 1738 to 1737.151 km.

The GRAIL detection of the third-degree Love number k_3 [*Konopliv et al.*, 2013; *Lemoine et al.*, 2013] is an impressive achievement. The strength of lunar tides falls off by 2 orders of magnitude per degree, but the shorter wavelengths for higher degrees help detection. Although GRAIL provides a degree-2 Love number accurate to 1%, at present the model values of higher-degree Love numbers (section 7) are expected to be more accurate than their measurements.

6. Lunar Rotation and Energy Dissipation

There are two known causes of energy dissipation in the Moon that affect lunar rotation and orientation, the physical librations: (1) Tidal distortion dissipates energy as the distortion varies due to changes in distance and apparent direction of the Earth. (2) The interactions at the two boundaries between fluid and solid material are weak, and the axis of rotation of the fluid core does not line up with the axis of the solid Moon

Table 5. Dissipation-Related Parameters From the DE430 Solution

Parameter	Function	Units	Value
K/C		1/d	$(1.64 \pm 0.17) \times 10^{-8}$
k_2		1	0.024059 fixed
Time delay Δt		day	0.0958 ± 0.0109
$\Delta\tau_{206}$	$\cos(2l - 2D)$	mas	1.54 ± 1.16
$\Delta\tau_{365}$	$\cos l'$	mas	5.00 ± 1.27
$\Delta\tau_{1095}$	$\cos(2F - 2l)$	mas	-3.64 ± 3.26
$\Delta I\sigma_{27.6}$	$\cos l$	mas	1.0 constrained

[*Goldreich*, 1967]. Dissipation arises from the fluid motion with respect to the mantle at the CMB and the motion at an inner core boundary. Lunar laser ranging detects both of these causes through their effects on the physical librations. This section updates the LLR dissipation solutions given by *Williams et al.* [2001]. GRAIL data analysis is likely to detect tidal dissipation as a phase shift in the largest monthly tidal variations, see Table 3 in *Konopliv et al.* [2013] for the nominal values used for GL0660B.

The equator of the Moon precesses retrograde along the ecliptic plane with a period of 18.6 years. The tilt between the equator and ecliptic planes is only $I = 1.543° = 0.02692$ radian. Although the Earth's much slower precession of the equatorial plane is along the ecliptic plane, this precession of the lunar equatorial plane follows the precession of the lunar orbit plane, but the tilt I is opposite to the orbit inclination. The synchronously rotating Moon is in a Cassini state [*Peale*, 1969]. The orientation of the lunar equatorial plane, and the pole normal to it, is not arbitrary; it depends on the inclination of the lunar orbit plane, the lunar gravity field including tides, CMB flattening, and dissipation from both tides and core boundary interactions [*Dickey et al.*, 1994; *Williams et al.*, 2001]. The change of orientation due to dissipation is large, 0.27″ in pole direction and −10.0″ in node, as determined by the LLR data analysis.

The weak interactions between the fluid and the mantle at the CMB leave the axis of rotation of the outer core close to the pole of the ecliptic plane [*Goldreich*, 1967], so the axes of the core and mantle differ by about I. The relative velocity at the CMB is approximately $R_f \omega \sin I$. The surface equatorial rotation rate is 4.62 m/s, so the differential velocity is about 25 mm/s for a CMB radius of about 20% of the lunar radius. The differential velocity at the inner core boundary would depend on its inclination to the ecliptic plane, which is not known.

Although the tidal time delay and the core boundary dissipation are both effective at introducing a shift in the precessing pole direction, the key to separating the two causes of dissipation is the detection of additional small physical libration effects of a few milliseconds of arc (mas) size. Guided by semianalytical theories for both tide and core boundary dissipation effects on physical librations [*Williams et al.*, 2001], the LLR data analysis solves for the coefficients of periodic terms in physical libration in longitude (τ) at 206 days, 1 year, and 1095 days in addition to a tidal time delay and the fluid core coupling parameter K/C. The three small periodic terms allow for tidal-dissipation-induced phase shifts in physical libration periodicities in addition to those implicit in the integrator models that use tidal time delay and K/C. From the solution leading to DE430, Table 5 gives the LLR-determined values for tide and core boundary dissipation parameters. In addition to the three terms correcting longitude libration τ, the solution constrains a latitude libration ($I\sigma$) correction at 27.555 day period. Uncertainties in the table are intended to include systematic and formal errors. The solution parameters for dissipation at the outer core boundaries (K/C) and tidal dissipation (time delay Δt) have a correlation coefficient of −0.908, but they are separated well enough that the detection of the fluid core is strong at nearly a factor of 10 greater than its uncertainty. The latitude libration correction is modeled as a circular correction to the path of the pole, so that the latitude libration coefficient for tilt $\Delta\rho$ is the same as for $\Delta I\sigma$ except for sign; e.g., the constrained $I\sigma$ correction is 1.0 mas cos I, whereas the $\Delta\rho$ correction is −1.0 mas sin I. The constrained correction is compatible with the step of the analysis that follows.

There are five solution parameters for lunar dissipation in Table 5: K/C, tidal time delay, and three longitude libration corrections. Orbit-related Delaunay arguments are l for lunar mean anomaly (27.555 day period); l' for solar, or Earth-Moon center of mass, mean anomaly (365.26 days); F for argument of latitude (27.212 days); and D for elongation of Moon from Sun (29.531 days). These angles are represented by polynomials in time and do not include periodic perturbations, see equation (5.43) in *Petit and Luzum* [2010]. Of the three longitude libration corrections, the annual correction is strongest compared with its uncertainty. The other two corrections are not strong compared with their uncertainties, but they are still useful for limiting frequency dependence of tidal dissipation.

The nominal model for lunar tides in the program that numerically integrates the lunar orbit and physical librations derives tidal accelerations and torques from equations (20) to (25) with **u** and r_p functions of time t minus a single time delay Δt [*Williams et al.*, 2001; *Standish and Williams*, 2012; *Folkner et al.*, 2014]. For tides, the Earth-Moon vector and the orientation of the Moon are computed at earlier time $t - \Delta t$, so that equation (20) is evaluated with $\mathbf{u}(t - \Delta t)$ and $r_p(t - \Delta t)$. Elastic tides would have $\Delta t = 0$, whereas a finite value introduces dissipation. The integrator does not use an expansion in Δt but consider the form that an expansion would have. The terms from $\mathbf{u}(t)$ and $r_p(t)$ would behave like elastic tides; the bulge would be aligned with the Earth, and the resulting forces would be radial and would apply no torques, but the moment of inertia matrix varies. Dissipative effects can come from the terms proportional to the product $k_2\Delta t$. These effects include secular changes in the orbit and tangential forces that cause torques, which can affect the lunar physical librations [*Williams et al.*, 2001]. With Q for the quality factor for dissipation, the energy dissipated during each tidal cycle depends on k_2/Q at the tidal period. For a tidal time delay, $k_2/Q = (2\pi k_2\Delta t)/\text{period} = (k_2\Delta t \text{ frequency})$. At 1 month, the Table 5 values give $(k_2/Q)_F = (2\pi k_2\Delta t)/(27.212 \text{ days}) = (5.3 \pm 0.6) \times 10^{-4}$ and $Q_F = 27.212 \text{ days}/(2\pi\Delta t) = 45 \pm 5$. Note that for the single time delay model of the integrator, each periodic term in a tidal expansion would have $k_2/Q \propto \text{frequency} \propto 1/\text{period}$.

If a single tidal time delay were a good fit to the dependence of tidal dissipation on frequency, then the 206 day, 365 day, and 1095 day corrections in Table 5 would be 0. The annual correction in Table 5 depends mainly on the annual tidal dissipation, making interpretation straightforward, whereas the two tidal dissipation terms at 206 days and 1095 days depend on tides at several periods [*Williams et al.*, 2001, Tables 1 and 2]. Using their Tables 3 (for constant Q) and 4 (time delay) gives an annual $(k_2/Q)_{365} = (6.4 \pm 1.5) \times 10^{-4}$ and, with the GRAIL k_2, $Q_{365} = 37 \pm 9$. In contrast to the single time delay model, which would have predicted an annual $(k_2/Q)_{365}$, an order of magnitude smaller, and a Q_{365} of hundreds, the Table 5 monthly and annual results, at periods different by a factor of 13.4, indicate that tidal k_2/Q and Q must have a much weaker dependence on tidal frequency. The uncertainties at 1 month and 1 year are too large to assess whether dissipation increases or decreases with period. The single time delay representation is not adequate, and we seek another form for k_2/Q. A k_2/Q that is independent of frequency can be tested by differencing Tables 3 and 4 in Williams et al. and multiplying by the above $(k_2/Q)_F = 5.3 \times 10^{-4}$. For the 1095 day correction, that procedure would give +10 mas amplitude, which does not have the right sign. A solution that approximately satisfies all five dissipation parameters in Table 5 requires adjusting K/C, $(k_2/Q)_F$, and the dependence of k_2/Q on tidal period.

Since the tidal frequency or period is not necessarily the same as the physical libration frequency or period, we need a relation for k_2/Q as a function of tidal period or frequency (2π/period). We posit a power law form for k_2/Q dependence on tidal period, $k_2/Q = (k_2/Q)_F \, (27.212 \text{ d/period})^{-w}$, with $(k_2/Q)_F$ and w parameters to be adjusted. For small cyclic distortions of materials, one expects energy dissipation per cycle to increase at lower frequencies or longer periods. Although the situation for the entire Moon is more complicated [*Efroimsky*, 2012a, 2012b], a positive w for tidal flexure would have been expected. Following *Williams et al.* [2001], we searched for a combination of fluid core K/C, $(k_2/Q)_F$, and w parameters that best satisfy the five Table 5 dissipation parameters. The result is $(k_2/Q)_F = (6.4 \pm 0.6) \times 10^{-4}$ and $w = -0.17 \pm 0.10$; with the GRAIL k_2, we obtain $Q_F = 37.5 \pm 4$. The fit of the five dissipation parameters is not as good as would be expected if the power law was a good representation. For example, the power law predicts that the annual k_2/Q is $(4.1 \pm 1.2) \times 10^{-4}$, plausibly agreeing with the $(k_2/Q)_{365} = (6.4 \pm 1.5) \times 10^{-4}$ found above, but not as good a match as one would like. Either the dissipation law is more complex or there are other unmodeled influences on physical librations.

Energy dissipation in the Moon may have affected early thermal evolution and helped to power a core dynamo. As the Moon evolved outward from Earth, there was a decrease in dissipated tidal and core-boundary power due to the increasing distance. However, at about 34 Earth radii, there was a change of Cassini state that caused the tilt of the lunar equatorial plane to the ecliptic and orbit planes to become large [*Ward*, 1975]. The power from both tidal and core-boundary dissipation increases with the tilt so near the Cassini state change, there was a surge of heat deposited in the mantle and at the boundaries between the outer fluid core and the adjacent solid core and mantle. *Williams et al.* [2001] suggested that the heat deposited at the two core boundaries could help power a dynamo. *Dwyer et al.* [2011] considered mechanical stirring of the core to be more efficient than thermal convection. Both mechanisms would link remanent magnetization found in lunar surface samples [*Garrick-Bethell et al.*, 2009; *Shea et al.*, 2012; *Suavet et al.*, 2013] with a core dynamo powered in part by the dissipation of energy from resonant or nearly resonant precession of the equatorial plane.

Table 6. Model Parameters and Love Numbers for Two Models of the Lunar Interior

Parameter	Weber et al. Model	Garcia et al. Model
R	1737.15 km	1737.15 km
R_f	330 km	380 km
R_i	240 km	0
M_f/M	6.4×10^{-3}	1.62×10^{-2}
M_i/M	6.3×10^{-3}	0
I_f/I_m	3.0×10^{-4}	7.7×10^{-4}
I_i/I_m	1.2×10^{-4}	0
k_2	0.0234	0.0223
h_2	0.0410	0.0390
l_2	0.0107	0.0104
k_3	0.00945	0.00910
h_3	0.0233	0.0224
l_3	0.00300	0.00298
k_{2f}	1.440	1.442
h_{2f}	2.440	2.442
l_{2f}	0.720	0.721

7. Model Calculations and Interior Structure

The Moon is believed to have a crust, a thick mantle, a fluid outer core, and probably a solid inner core. The crust makes up the top 2–3% of the lunar radius, the thick mantle accounts for at least 75%, and the outer core radius is within a few percent of 20%. At the base of the mantle, above the outer core, is a layer of low seismic Q and low shear velocity often thought to be partially molten. Deep-focus moonquakes occur in the region immediately above the low-velocity layer. See *Wieczorek et al.* [2006] for a review covering knowledge of the interior. Interior elastic properties are clues to composition. Given radial profiles of density and seismic P and S wave velocities, the elastic Love numbers can be computed. In this section we use profiles from two recent lunar models to compute Love numbers. Model Love numbers are also computed for variations on the interior models that include different outer core radii. The model values are then compared with the density, moment of inertia, and Love number determinations given in sections 2 and 5. A new sequence of interior models that satisfy these values is constructed, and their sensitivity to core and crustal densities is assessed.

The structure of the outer ~60% of the Moon by radius comes from the analyses of the Apollo seismic data. There are a number of concordant analyses. Two published models are discussed below. Nonseismic evidence for a lunar core comes from moment of inertia, magnetic induction, and lunar laser ranging. The moment of inertia indicates that density generally increases with depth. Magnetic induction indicates an electrically conductive core but does not determine the state; *Hood et al.* [1999] gave a radius of 340 ± 90 km, whereas *Shimizu et al.* [2013] found a radius of 290 km with an upper bound of 400 km. Analysis of lunar orientation, the physical librations determined from LLR data, indicates two sources of dissipation: tides and an interaction at a fluid-core/solid-mantle boundary. *Williams et al.* [2001] detected a fluid core and placed a 374 km upper limit on the radius if the core density matches that of an Fe-FeS eutectic fluid, or a 352 km upper limit for a pure iron composition. The LLR dissipation analysis is updated in section 6. Table 3 includes an LLR detection of the outer core flattening, another interaction requiring a fluid outer core. Presumably, the lunar core is composed of iron and siderophile elements.

Two recent models of the Moon's deep interior come from *Weber et al.* [2011] and *Garcia et al.* [2011]. Both models are based on the analyses of the Apollo seismic data plus mean density. Garcia et al. also used information on mean moment and Love number. In both analyses, the outer radius of the fluid outer core was estimated from the arrival times of reflected seismic waves. Weber et al. obtained $R_f=330\pm20$ km for the fluid core radius, whereas Garcia et al. obtained $R_f=380\pm40$ km. Weber et al. also identified possible reflections off the inner core boundary and the top of a low-velocity layer at the base of the mantle. The two radii were given as $R_i=240\pm10$ km and $R_{lv}=480\pm15$ km, respectively. These radius determinations are affected by seismic velocities above the interfaces. Garcia et al. did not report an inner core or a low-velocity layer, and neither feature is present in their model. The model differences in the deep mantle and core illustrate uncertainties in deep lunar structure and properties. High attenuation in the deep mantle weakens the seismic signals and limits knowledge of the deep interior.

The model degree-2 and -3 elastic Love numbers and the degree-2 fluid Love numbers (subscript f) calculated from the *Weber et al.* [2011] and *Garcia et al.* [2011] models are given in Table 6. Also given are the inner and outer core mass and moment fractions. Both published models used a lunar radius of 1737.1 km, which has been expanded to 1737.15 km in the calculations here, and both models have a 40 km thick crust with an average density close to 2760 kg/m^3. Small adjustments $<0.3\%$ were made to both density profiles to

Table 7. Parameter Extremes and Love Number Expressions for Variations on Two Models of the Lunar Interior

Parameter	Weber et al. Model Variations	Garcia et al. Model Variations
R_f	278–372 km	276–367 km
R_i	277–0 km	275–0 km
M_f/M	0.0001–0.0150	0.0001–0.0146
M_i/M	0.0097–0	0.0095–0
I_f/I_m	$0–6.9\times10^{-4}$	$0–6.5\times10^{-4}$
I_i/I_m	2.5×10^{-4}–0	2.5×10^{-4}–0
k_2 span	0.0231–0.0237	0.0214–0.0221
k_2 solid Fe core	0.0226	0.0210
$k_2(R_f)$	$0.02270\,[1+4.64\,(R_f/R)^3]$	$0.02076\,[1+6.98\,(R_f/R)^3]$
$h_2(R_f)$	$0.03965\,[1+4.67\,(R_f/R)^3]$	$0.03621\,[1+7.14\,(R_f/R)^3]$
$l_2(R_f)$	$0.01069\,[1+0.39\,(R_f/R)^3]$	$0.01034\,[1+0.53\,(R_f/R)^3]$

match the mean density and solid moment $I_s/MR^2 = 0.393112$ of this paper for $R = 1737.151$ km (sections 2 and 5). Among the geophysical parameters fit for their model, Garcia et al. used a low k_2 value, an older and less accurate LLR value, than the GRAIL-derived values in Table 4, and that choice contributed to a more rigid model. For the Weber et al. model, the degree-2 Love numbers in the table are very similar to the model values given in that paper, but the GRAIL-derived k_2 values are larger than the model values. The GRAIL results constrain possible lunar models. For both models, the combined inner and outer core makes up less than 2% of the lunar mass.

The degree-2 Love numbers in Table 6 are ~1% different from those given by *Weber et al.* [2011] and *Garcia et al.* [2011]. Weber et al. gave $k_2 = 0.0232$ and $h_2 = 0.0406$, whereas Garcia et al. gave $k_2 = 0.0223$, $h_2 = 0.0394$, and $l_2 = 0.0106$. There can be small differences in the analysis procedures, and there are small differences (<0.3%) in the density distributions that were forced to match this paper's mean density and solid moment of inertia.

Variations on both lunar models were generated by simultaneously changing the radii of the fluid outer core and solid inner core while requiring the lunar mean density and solid moment of inertia to be satisfied. One extreme has a vanishingly small inner core with a maximum size outer core, whereas the other extreme has only a very thin shell of fluid between the mantle and inner core, giving a maximum size inner core and a minimum size outer core. For the *Garcia et al.* [2011] model, the variation required the addition of a solid inner core with the density of iron (8000 kg/m^3). These model variations are summarized in Table 7. The extreme fluid core radii for variations on the *Weber et al.* [2011] model are 278 km (thin fluid layer) and 372 km. For the Garcia et al. variations, the extreme radii are 277 km and 367 km. These extremes were found by requiring the moment of inertia of the input density profile to agree closely with the I_s/MR^2 found in this paper. For Garcia et al., the 367 km maximum is smaller than their 380 km radius due to the different moment of inertia of this paper. On the basis of the extreme cases, the table presents fits to the model k_2, h_2, and l_2 Love numbers as a function of the cube of the ratio of the fluid core radius to the lunar radius, R_f/R. These empirically derived cubic expressions were tested on intermediate points. From these expressions, the fluid outer core in the Weber et al. model contributes 3% to the k_2 and h_2 Love numbers, whereas the larger core of Garcia et al. contributes 7%. The l_2 Love number is an order of magnitude less sensitive to the outer core size. Unlike the terrestrial planets with their large fluid cores, the small lunar core has only a subtle influence on the tidal response.

The expressions in Table 7 show that Love numbers increase with a larger fluid core. In addition, they also increase with a smaller mantle *S* wave velocity. The existing seismic data are not able to determine the lower mantle *S* wave velocity as well as the velocity in the middle and upper mantle. The *Garcia et al.* [2011] Love numbers are lower than the *Weber et al.* [2011] values despite the larger fluid core in the former model, because that model lacks an *S* wave low-velocity layer at the base of the mantle.

The model k_2 values in Tables 6 and 7 are lower than the GRAIL-derived value. What modifications to the lunar interior models would allow the average GRAIL-determined Love number to be fit better? With the average $k_2 = 0.02422 \pm 0.00022$ from section 5, we can solve the cubic relation of Table 7 to obtain $R_f = 423 \pm 21$ km for the Weber et al. variations, which is larger than any radius in Table 7. The cubic relation for the Garcia et al. model variations gives $R_f = 500$ km, which is even larger. Another change is needed. Increasing the *Weber et al.* [2011] 480 km radius of the low-velocity zone by 20 km increases k_2 by 0.0001, whereas decreasing the *S* wave velocity by 500 m/s increases k_2 by 0.0003. Applying both changes to the model, an outer core radius of $R_f = 380$ km satisfies the GRAIL-determined Love number, consistent with the *Garcia et al.* [2011] estimate of core radius. Although the core radius is larger than the proposed Weber et al. radius, it is compatible with the

Table 8. GRAIL Primary Mission (GPM) Models That Satisfy Mean Density, Mean Solid Moment, Love Number, and a Deep Mantle Low-Velocity Zone[a]

Parameter	GPM1	GPM2	GPM3	GPM4	GPM5
R_f	372 km	350 km	325 km	300 km	278 km
R_i	0	183 km	230 km	259 km	277 km
R_{lv}	507 km	520 km	534 km	545 km	554 km
M_f/M	0.0150	0.0107	0.0064	0.0028	0.0001
M_i/M	0	0.0028	0.0055	0.0079	0.0097
I_f/I_m	6.9×10^{-4}	4.9×10^{-4}	2.9×10^{-4}	1.2×10^{-4}	2.9×10^{-6}
I_i/I_m	0	3.1×10^{-5}	9.7×10^{-5}	1.8×10^{-4}	2.5×10^{-4}
I_m/MR^2	0.39338	0.39330	0.39322	0.39316	0.39311
k_2	0.02422	0.02422	0.02422	0.02422	0.02422
h_2	0.04237	0.04237	0.04240	0.04240	0.04242
l_2	0.01076	0.01077	0.01077	0.01078	0.01079
k_3	0.00951	0.00952	0.00952	0.00953	0.00954
h_3	0.02344	0.02345	0.02348	0.02350	0.02353
l_3	0.00298	0.00298	0.00298	0.00298	0.00297
k_4	0.00536	0.00537	0.00537	0.00537	0.00537
k_{2f}	1.441	1.441	1.440	1.439	1.439
h_{2f}	2.441	2.441	2.440	2.439	2.439
l_{2f}	0.721	0.720	0.720	0.720	0.719

[a]The reference $R = 1737.15$ km.

results of other techniques. There is a family of models that can be formed by adjusting the radii of the inner and outer core and including a low-velocity layer. For the Garcia et al. model, a low-velocity layer is needed above the core to increase its Love number.

The fluid core density deserves comment. The *Weber et al.* [2011] and *Garcia et al.* [2011] models have an outer core density appropriate to a near-eutectic Fe-FeS composition at a pressure of 5 GPa [*Brett and Bell*, 1969; *Brett*, 1973; *Usselman*, 1975; *Sanloup et al.*, 2000, 2002]. Weber et al. used 5100 kg/m^3, whereas Garcia et al. used 5171 kg/m^3. The solidification of a solid iron inner core from an iron-rich Fe-S melt would concentrate the sulfur in the fluid while lowering its density and freezing point [*Stevenson and Yoder*, 1981]. An initial iron-rich melt would evolve toward the eutectic mixture. See *Brett and Bell* [1969], *Sanloup et al.* [2002], and *Chen et al.* [2008] for the relevant phase curves. Initial iron-rich melts are plausible; models with a fluid density larger than the eutectic value are explored below. Other elements can also be present in the melt, including nickel, carbon [*Hirayama et al.*, 1993], and various siderophile elements. In contrast to an iron-rich core, a molten silicate core rich in ilmenite would have a much lower density of ~3500 kg/m^3 [*Wieczorek and Zuber*, 2002; *Wieczorek et al.*, 2006].

All-solid models with a solid iron core predict lower Love numbers. If the thin-shell modification of the Weber et al. model (Table 7) is converted to a completely solid core by removing the liquid shell, then the Love number decreases from 0.0231 to 0.0226. For the modified Garcia et al. profile, the Love number decreases from 0.0214 to 0.0210. The thin fluid shell case does not give the same Love numbers as a completely solid core. Even a thin shell of fluid gives larger Love numbers than a completely frozen core. All-solid iron core models have Love numbers that are lower than the GRAIL determinations by 7% (Weber et al.) and 13% (Garcia et al.). Layered solid core models were not investigated, but presumably, they would also have low Love numbers compared with their fluid-outer/solid-inner core analogs. Lower density solid cores were also not investigated. Whereas the model k_2 can be increased by expanding the size or lowering the seismic wave speed in the low-velocity zone, the resulting model would feature a core that is sufficiently cool to freeze juxtaposed against a lower mantle that is sufficiently hot to be attenuating and perhaps partially molten. A completely solid iron core offers no advantages, and it conflicts with the LLR and seismic evidence for a fluid outer core.

Five GRAIL Primary Mission (GPM) models that are modifications of the *Weber et al.* [2011] model are summarized in Table 8. They satisfy the mean density 3345.56 kg/m^3, the mean solid moment of inertia $I_s/MR^2 = 0.393112$, and the GRAIL-derived Love number $k_2 = 0.02422$. The Weber et al. densities were maintained for the GPM models, but the inner and outer core radii were adjusted to satisfy the mean density and solid moment values. Figures 1–3 show the spread of GPM model values for radii, mass fractions, and moment fractions. Figure 1 displays radii for the inner and outer core. Figure 2 gives the mass fractions M_f/M and M_i/M plus their sum. Figure 3 gives the moment fractions I_f/I_m and I_i/I_m. Note that the GPM3 model has inner and outer core radii

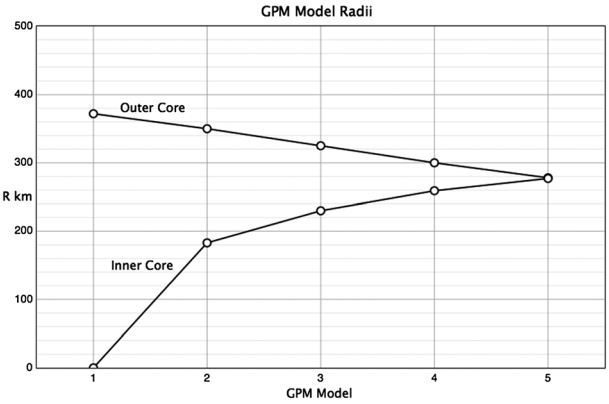

Figure 1. Radii of inner and outer core for five GPM models.

of 230 km and 325 km that match the *Weber et al.* [2011] values within the uncertainties that were proposed for those radii, 240 ± 10 km and 330 ± 20 km, respectively. The GPM3 model's density and seismic velocity profiles are shown in Figure 4.

After adjusting the core radii, the outer radius of the low-velocity zone was adjusted until the GRAIL-determined k_2 was matched. For the low-velocity zone, the *S* wave velocity of $V_S = 2700$ m/s is 500 m/s lower than in the *Weber et al.* [2011] model, the *P* wave velocity of $V_P = 7160$ m/s is 340 m/s lower, and the zone's outer radius is larger. An increased outer radius for the low-velocity zone could be replaced with a lower *S* wave velocity. This initial fit to the GRAIL-derived k_2 with a low-velocity layer will be replaced with a viscoelastic model in the next section.

The GPM1 model resembles the *Garcia et al.* [2011] model with the addition of a low-velocity layer. However, the Garcia et al. near-eutectic Fe-FeS outer core composition and density are compatible with an inner core. A model in the spread from $372 \geq R_f \geq 340$ km and $0 \leq R_i \leq 205$ km would still satisfy the Garcia et al. $R_f = 380 \pm 40$ km value.

The Love numbers are given to more significant figures in Tables 7 and 8 than a 1% accuracy would justify. An extra digit is useful for comparing differences among models. The 1% uncertain GRAIL-derived k_2 and the 1% model computational accuracy will influence the size of the low-velocity layer rather than the core radii.

The models in Table 8 are not unique. There is a family of models that satisfy the known data. Considering small possible model adjustments to the density profile of the mantle, and larger density adjustments possible for crust and core, there would be a broader spread of acceptable model values than those shown in Table 8.

The GPM models were generated by adjusting the Weber et al. inner and outer core radii and the radius of the low-velocity layer. The *S* wave velocity in the low-velocity layer was also reduced. All densities were held constant. How do different crustal or outer core densities affect the results in Table 8? Table 9 addresses this question by showing the end-members of models that satisfy the mean density, moment of inertia, and Love number. *Wieczorek et al.* [2013] used the GRAIL gravity field data and the Lunar Orbiter Laser Altimeter (LOLA) topography data to infer an upper crustal density of 2550 kg/m^3 and an average crustal thickness of 34 to 43 km. For a model perturbation, here we decrease the density of the three-layer Weber et al. crust by 183 kg/m^3 for an average of 2577 kg/m^3 over the 40 km thickness. This 7% decrease in the crustal mass was compensated by a 0.7% increase in density for the rest of the Moon. Model Love numbers are nearly the same as those in Table 8, but the l_2 values are slightly smaller (0.01070–0.01072). Changing the thickness of the crust would also change its mass. A thickness of 34 to 43 km corresponds to a −15% to +8% volume change, with the mass difference depending on the density distribution. Although the crust's mass is still uncertain, it is clear that decreasing the crustal density or changing the crustal thickness can introduce shifts of many tens of kilometers to the model's inner and outer core radii.

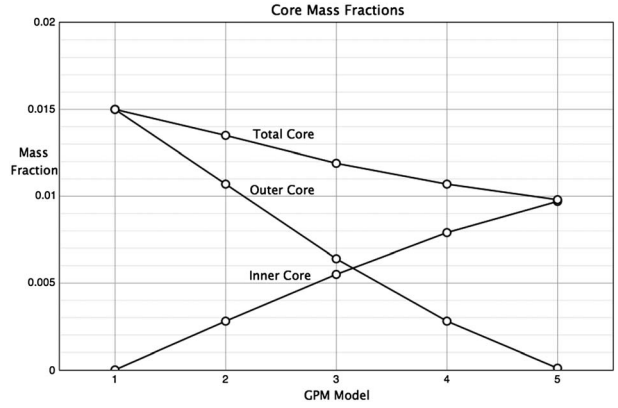

Figure 2. Inner and outer core mass fractions M_i/M and M_f/M plus their sum for five GPM models.

The choice of the Fe-FeS eutectic density for the GPM models implies that the fluid

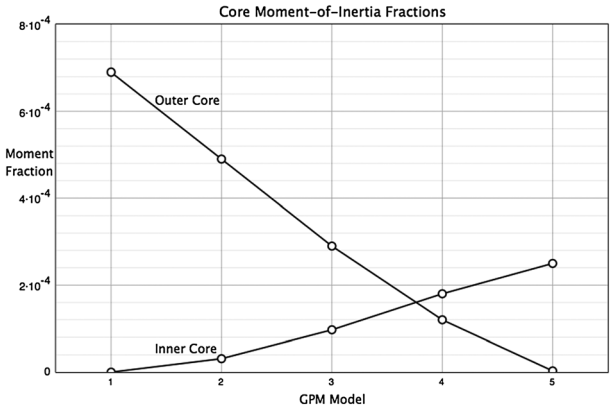

Figure 3. Inner and outer core moment of inertia fractions I_i/I_m and I_f/I_m for five GPM models.

evolved toward the ~1000°C minimum temperature of the eutectic, while the solid core grew. If the core is hotter, then the fluid may be more iron rich and dense than the eutectic composition. Decreasing the sulfur content from the 25 wt % of the eutectic composition to 10 wt % increases the density to about 5700 kg/m^3 [*Sanloup et al.*, 2000]. The boundary between solid and liquid then occurs at temperatures approaching 1500°C [*Brett and Bell*, 1969]. This case is shown in the last column of Table 9. The maximum outer core size is reduced by 32 km, but the thin-shell minimum remains the same. Model Love numbers are very close to those in Table 8. A fully liquid iron core for the Moon, not investigated here, would require core temperatures of ~1660°C [*Brett*, 1973]. Such a high core temperature is not expected at the present time, since models of lunar cooling have lower temperatures at the base of the mantle; the calculations by *Spohn et al.* [2001] indicate a lower mantle temperature that is 200–250° cooler, whereas the model of *Ziethe et al.* [2009] is nearly 500° cooler.

Opposite to a higher density iron-rich core, the low-density ilmenite-rich silicate fluid core of *Wieczorek and Zuber* [2002], which was discussed at greater length by *Wieczorek et al.* [2006], requires a 460 km radius to match the GRAIL k_2 value or a 583 km radius to match the new density and moment, both using the Weber et al. crust and mantle densities without a lower mantle low-velocity layer. The former radius is a poor match to the moment of inertia, and the latter radius gives a k_2 value of 0.0273, 13% larger than the GRAIL determination. Note that the moonquake zone, approximately 800–1100 km deep as given by *Goins et al.* [1981] or possibly extending somewhat deeper according to *Nakamura* [2005], provides an upper limit to the size of the fluid core. A smaller core radius would result from an increase in the mantle's density with depth. To satisfy this paper's density, moment, and Love number values, low-density core models would require modifications to crustal and mantle density that are not explored here.

The deep structure of the Moon is uncertain, but a consistent picture can be painted. Subject to this paper's values for mean density and moment of inertia, a range of inner and outer core radii are possible. In the GPM models (Table 8), the outer core composition is assumed to have approached the Fe-FeS eutectic composition from the iron-rich side, but additional siderophile elements could be present. A plausible range for the fluid outer core radius is about 200–380 km, guided by the ranges in Table 9 contributed by uncertainties in lunar model densities. Iron plus other less abundant elements that have solidified from the melt would make an inner core with radius less than approximately 280 km and mass fraction ≤1%. The combined inner and outer core mass fraction is ≤1.5% for the models of Tables 7–9. Lunar models would benefit from a reanalysis of the seismic data subject to the new values for density, moment of inertia, and Love number.

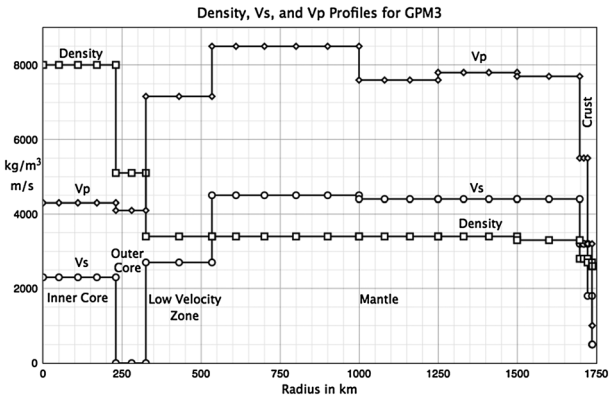

Figure 4. Profiles of lunar density in kg/m^3 and seismic speeds V_S and V_P in m/s versus radius for model GPM3.

8. Viscoelastic Models and Love Numbers

The analysis of lunar laser ranging data shows strong tidal dissipation in the Moon [*Williams et al.*, 2001]. Subsequent solutions continue to support strong tidal dissipation; an update in section 6 finds monthly $(k_2/Q)_F = (6.4 \pm 0.6) \times 10^{-4}$

Table 9. Parameter Spreads for GPM Models Plus Separate Model Variations With a Lower Density Crust and a Higher-Density Outer Core

Parameter	GPM 1–5	Less Dense Crust	More Dense Outer Core
R_f	372 – 278 km	301 – 222 km	340 – 278 km
R_i	0 – 277 km	0 – 221 km	0 – 277 km
R_{lv}	507 – 554 km	550 – 576 km	525 – 553 km
M_f/M	0.0150 – 0.0001	0.0079 – 0.0001	0.0128 – 0.0001
M_i/M	0 – 0.0097	0 – 0.0049	0 – 0.0097
I_m/MR^2	0.39338 – 0.39311	0.39321 – 0.39311	0.39330 – 0.39311

or, with the GRAIL-determined k_2, $Q_F = 37.5 \pm 4$. The LLR data analysis is sensitive to tidal periods from 0.5 month to 6 years and indicates that tidal k_2/Q decreases with period, which is contrary to usual expectations for a rocky body. As a consequence of tidal dissipation, models by *Efroimsky* [2012a, 2012b] and *Nimmo et al.* [2012] predict that Love numbers depend on period. We seek an expression for elastic properties as functions of period that can be used to link the monthly GRAIL k_2 determinations with local seismic velocities near 1 s period. Then the monthly k_2 and k_2/Q values can be extended to other periods.

Information on dissipation at seismic frequencies has long been known. The analysis of Apollo seismometer data led to the discovery of an attenuating layer of low seismic velocities in the deep mantle [*Nakamura et al.*, 1973, 1974, 1976; *Nakamura*, 1983; *Toksöz et al.*, 1974; *Goins et al.*, 1981]. This layer, just above the core, was suspected to be a zone of partial melting. The upper and middle mantle also dissipate seismic energy but less strongly than the deep low-velocity zone. Values of the dissipation-related quality factor Q for the upper mantle are several thousand [*Nakamura and Koyama*, 1982].

The local S wave velocity V_S is given by $V_S^2 = \mu/\rho$, where μ is the shear modulus or rigidity and ρ is the density. All the three parameters vary with radius within the Moon. S wave attenuation is associated with μ rather than ρ, and if μ is represented with a complex variable, then the imaginary part expresses the dissipative component. Laboratory experiments have explored the frequency dependence of rigidity and associated dissipation [*Gribb and Cooper*, 1998; *Jackson and Faul*, 2010]. For a small distortion at a period P, we use a combination of an Andrade power law representation and Maxwell viscosity. The power law controls the short-period dissipation, whereas a viscous term would dominate the long-period dissipation.

$$\frac{1}{\mu(P)} = \frac{1}{\mu(0)} + b\cot\left(\frac{w\pi}{2}\right)\left(\frac{P}{P_r}\right)^w - i\left[b\left(\frac{P}{P_r}\right)^w + \left(\frac{P}{2\pi\eta}\right)\right]. \tag{28}$$

Here P_r is a reference period, b combines a parameter that depends on the material with functions of P_r and exponent w, and η is shear viscosity. The ratio of the (negative) imaginary and real parts gives the tangent of the phase shift. We take the sine of the phase shift as equal to $1/Q$. See *Efroimsky* [2012a, 2012b] for a discussion of several definitions of Q. It is not clear whether a viscosity term is needed for deep lunar conditions. As $\eta \to \infty$, expression (28) approaches an anelastic representation.

The Love number k_2 for a homogeneous incompressible sphere can be written as $3/[2(1 + 19V_S^2/V_e^2)]$, where V_e is the escape velocity at the surface. For the Moon, $V_S \approx 4.4$ km/s and $V_e = 2.38$ km/s, so $19V_S^2/V_e^2 \approx 65$. The 3/2 factor is replaced by 5/2 for displacement Love number h_2 and by 3/4 for l_2. For small nearly homogeneous bodies with weak gravity, the Love number is approximately proportional to $1/\mu$ and equation (28) may be used to approximate a frequency-dependent Love number by multiplying equation (28) by $3\rho V_e^2/38$. Even when there is internal structure, equation (28) suggests a form for a frequency-dependent Love number.

$$k_2(P) = k_2(P_F) + K\cot\left(\frac{w\pi}{2}\right)\left[\left(\frac{P}{P_F}\right)^w - 1\right] - i\left[K\left(\frac{P}{P_F}\right)^w + \xi\left(\frac{P}{P_F}\right)\right]. \tag{29}$$

We have substituted $P_r = P_F$, where $P_F = 27.212$ days, and $k_2(0) = k_2(P_F) - K\cot(w\pi/2)$, to make the right-hand side of equation (29) depend on a monthly reference period. The viscous parameter ξ depends on $1/\eta$ and several other parameters, including the fraction of the real Love number that comes from the layer exhibiting viscosity, presumably the low-velocity zone. The negative imaginary part depends on period and is identified with k_2/Q.

Although equation (29) can be approximated from equation (28) for a small homogeneous body and guessed for small layered bodies, it can also be derived for larger structured bodies by adding together the fraction of k_2 that comes from each layer, provided that w is assumed to be the same for all the dissipative layers. To construct an anelastic Earth model, *Wahr and Bergen* [1986] used partial derivatives of k_2 with respect to μ times $\mu(P) - \mu(P_r)$ from two mantle layers. Bulk modulus was treated similarly. The resulting analogue of equation (29), but with $\xi = 0$ and a different reference period, is applied to tidal dissipation in the solid Earth, see equation (6.12) in *Petit and Luzum* [2010]. Partials of k_2 with respect to μ were also used by *Khan et al.* [2004] in their investigation of lunar Q.

For a structured body, equation (29) for $k_2(P)$ can be assembled from equation (28) by using a Taylor series truncated following the linear terms. In particular, by summing the partial derivative of $k_2(P_r)$ with respect to $\mu_j(P_r)$ for each lunar layer j times $\mu_j(P) - \mu_j(P_r)$ from equation (28) for that layer, for $P_r = 0$, the expansion is

$$k_2(P) = k_2(0) + \sum_j \frac{\partial k_2(0)}{\partial \mu_j(0)} \left[\mu_j(P) - \mu_j(0)\right]. \tag{30}$$

Multiplying by $-\mu_j(0)^2$ converts the partial derivative with respect to $\mu_j(0)$ into a partial derivative with respect to $1/\mu_j(0)$, which is appropriate for use with equation (28):

$$k_2(P) = k_2(0) - \sum_j \mu_j(0) \frac{\partial k_2(0)}{\partial \mu_j(0)} \left[\frac{\mu_j(0)}{\mu_j(P)} - 1\right]. \tag{31}$$

The lunar Love numbers are only slightly affected by bulk modulus, so those partial derivatives are ignored in our approximation. With $\mu = 0$ for a fluid, the outer core contributes to $k_2(0)$, but dissipation there depends only on bulk modulus and that partial derivative is disregarded here. We may substitute equation (28) into equation (31) to obtain the compact form of equation (29), provided that all the layers have the same exponent w. Otherwise, there would be multiple terms. Expressions for the displacement Love numbers h_2 and l_2 follow the same form as equation (29). Very long periods or very small values of Q would require terms in addition to the linear expansion.

If equation (28) is substituted into (31) with the same exponent w for all the layers, then one derives equation (29) with the following expressions for K and ξ:

$$K = -\sum_j \frac{\partial k_2(0)}{\partial \mu_j(0)} \mu_j(0)^2 b_j \tag{32}$$

$$\xi = -\sum_j \frac{\partial k_2(0)}{\partial \mu_j(0)} \frac{\mu_j(0)^2 P_F}{2\pi\eta_j}. \tag{33}$$

Note that $\eta_j/\mu_j(0)$ is the Maxwell time for layer j. Analogous to equation (29), expressions for $h_2(P)$ and $l_2(P)$ result from replacing $\partial k_2(0)/\partial \mu_j(0)$ in equations (30)–(33) with $\partial h_2(0)/\partial \mu_j(0)$ and $\partial l_2(0)/\partial \mu_j(0)$. That substitution generates parameters analogous to K and ξ.

Since $\mu = \rho V_S^2$, analysis of lunar seismic data for a band of periods near 1 s supplies information on the internal structure along with $\mu(r)$ at seismic periods [*Goins et al.*, 1981; *Nakamura*, 1983; *Weber et al.*, 2011; *Garcia et al.*, 2011]. The imaginary part of equation (29) is zero at zero period. We assume that dissipation-free values of $k_2(0)$, $h_2(0)$, and $l_2(0)$ can be calculated for the five GPM models by replacing the seismic V_S and V_P of the low-velocity zone with the adjacent mantle values of $V_S = 4500$ m/s and $V_P = 8500$ m/s. Zero-period values $k_2(0)$, $h_2(0)$, and $l_2(0)$ are presented in Table 10 for the five models.

The partial derivatives of the lunar Love numbers with respect to μ are presented in Table 11 for each layer j in the GPM3 model. Since $V_S^2 = \mu/\rho$ and $V_P^2 = K_S/\rho + (4/3)V_S^2$, where K_S is adiabatic bulk modulus, the partial derivatives were computed from finite difference perturbations of the seismic velocities, decrementing V_S^2 by 10% and V_P^2 by 10% of $(4/3)V_S^2$. The nominal values of the parameters were at their zero-period values, so the $\mu_j(0)\partial k_2(0)/\partial \mu_j(0)$ are suitable for equations (31)–(33). Except for sign, dividing by $k_2(0)$ ideally gives the fraction of $k_2(0)$ contributed by each layer. Since the partial derivatives are generated from finite differences rather than infinitesimals, the sum of each column differs somewhat from -1. Although the layers have different thicknesses, a column-by-column comparison can be made. The sensitivities of the k_2 and h_2 partial derivatives with respect to μ in the different layers are similar, with h_2 slightly more sensitive to deep

Table 10. Parameters for Frequency-Dependent GPM Models

Parameter	GPM1	GPM2	GPM3	GPM4	GPM5
$k_2(0)$	0.02313	0.02289	0.02265	0.02245	0.02229
$h_2(0)$	0.04038	0.03995	0.03952	0.03916	0.03888
$l_2(0)$	0.01070	0.01069	0.01068	0.01067	0.01067
$[V_{Slv}^2/(R_{lv}-R_f)]\cdot\partial k_2/\partial(V_{Slv}^2)$	-1.00×10^{-5}/km	-0.94×10^{-5}/km	-0.89×10^{-5}/km	-0.83×10^{-5}/km	-0.79×10^{-5}/km
$[V_{Slv}^2/(R_{lv}-R_f)]\cdot\partial h_2/\partial(V_{Slv}^2)$	-1.82×10^{-5}/km	-1.72×10^{-5}/km	-1.62×10^{-5}/km	-1.53×10^{-5}/km	-1.45×10^{-5}/km
$[V_{Slv}^2/(R_{lv}-R_f)]\cdot\partial l_2/\partial(V_{Slv}^2)$	-5×10^{-7}/km	-5×10^{-7}/km	-5×10^{-7}/km	-5×10^{-7}/km	-5×10^{-7}/km
w for $\xi=0$	0.338	0.286	0.246	0.221	0.204
w for $\xi=10^{-6}$	0.338	0.285	0.246	0.221	0.204
w for $\xi=10^{-5}$	0.334	0.282	0.243	0.218	0.201
w for $\xi=10^{-4}$	0.293	0.246	0.211	0.189	0.174

structure. In contrast, l_2 is much more sensitive to the layers in the outer half of the lunar radius. The cubic expressions for the Love numbers in Table 7 show that l_2 is an order of magnitude less sensitive to the outer core than are k_2 and h_2, analogous to the partial derivatives for the low-velocity layer.

The partial derivatives in Table 11 can be used to relate the tidal Q to the Q_j associated with $1/\mu_j$ for layer j. If $Q_j(P_F) \gg 1$ and $\mu_j(P_F) \approx \mu_j(0)$, then the monthly dissipation has $1/Q(P_F) \approx -\sum[\mu_j(0)/k_2(0)]\,[\partial k_2(0)/\partial\mu_j(0)]/Q_j(P_F)$. If all of the tidal dissipation is coming from the low-velocity zone at the base of the mantle, then $Q_{lv} \approx 3$ at 1 month, which strains the $Q_j \gg 1$ requirement. If the tidal dissipation is split evenly between the two lowest mantle layers, then the local Q values are ~6 and ~29 at 1 month.

There are four parameters on the right-hand side of equation (29) that must be specified. The Love number $k_2(P_F) = 0.02422 \pm 0.0022$ results from GRAIL data analysis, $K + \xi = (k_2/Q)_F = (6.4 \pm 0.6)\times10^{-4}$ is determined by LLR data analysis (section 6), and w and ξ depend on the GPM models. We select a sequence of ξ values and solve for w: (1) $K = (k_2/Q)_F - \xi$ and (2) $w = (2/\pi)\tan^{-1}\{K/[k_2(P_F) - k_2(0)]\}$. For a given value of ξ, there is a unique value of w for each GPM model. The anelastic case has $\xi = 0$.

The solutions for exponent w are presented in Table 10. They are computed for four values of the ξ parameter for each of the five GPM models. The values of w in Table 10 range from 0.17 to 0.34. For solid-body Earth tides, the *Wahr and Bergen* [1986] expression with the form of equation (29), but with $\xi = 0$, is used with $w = 0.15$ [*Petit and Luzum*, 2010]. Laboratory experiments on polycrystalline olivine by *Gribb and Cooper* [1998] and *Jackson and Faul* [2010] indicated w values of 0.35 and 0.34, respectively. Two cautions are needed: the laboratory data were obtained at subdaily periods and the low Q values are less reliable. *Nimmo et al.* [2012] used an extended Burgers model, a sophisticated computation that depends on diffusion and grain boundary sliding. They replaced equation (28) with integral expressions, but the anelastic form of equation (29) fits their baseline model for tidal periods fairly well, except that their multiyear k_2/Q values increase more slowly than an anelastic $(P/P_F)^w$ power law would predict.

Also presented in Table 10 are the partial derivatives of $k_2(0)$, $h_2(0)$, and $l_2(0)$ with respect to V_S^2 for the mantle layer adjacent to the core, given a modification to the "low-velocity" zone achieved by setting $V_S = 4500$ m/s and $V_P = 8500$ m/s for zero period. The partial derivatives were derived from a -10% change of $V_S^2 = (4500\ \text{m/s})^2$ in a low-velocity zone with radii R_{lv} from Table 8 in the previous section. Dividing by R_{lv}-R_f partly compensates for the different radial extents for the low-velocity layer in the five GPM models; the partials may be multiplied by

Table 11. For Parameters at Zero Period, the Partial Derivatives of Love Numbers With Respect to Shear Modulus μ Are Tabulated for Each Layer in the GPM3 Model

Layer	Layer Radii	$(\mu/k_2)\,\partial k_2/\partial\mu$	$(\mu/h_2)\,\partial h_2/\partial\mu$	$(\mu/l_2)\,\partial l_2/\partial\mu$
Inner core	0 – 230 km	0	0	0
Outer core	230 – 325 km	0	0	0
Low velocity	325 – 534 km	−0.082	−0.086	−0.009
Mantle	534 – 999 km	−0.392	−0.401	−0.164
Mantle	999 – 1249 km	−0.261	−0.259	−0.252
Mantle	1249 – 1499 km	−0.204	−0.188	−0.374
Mantle	1499 – 1697 km	−0.091	−0.069	−0.273
Crust	1697 – 1737 km	−0.004	−0.001	−0.020

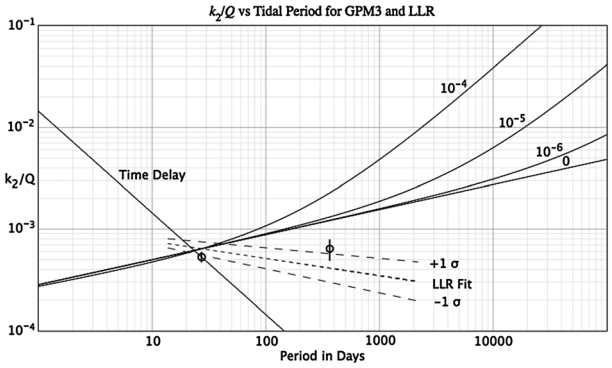

Figure 5. Model k_2/Q values versus tidal period for the GPM3 model (solid curves with positive slope). The viscosity-related parameter ξ has values of 0, 10^{-6}, 10^{-5}, and 10^{-4}. The dashed lines show the multiterm LLR determination and ±1σ uncertainties from 0.5 month to 6 years. The circles mark the LLR determinations at 1 month and 1 year. A time delay model fits dissipation only at 1 month.

alternative thicknesses or V_S^2 values. As an example, the *Weber et al.* [2011] radius for the low-velocity zone is 480 km, and the outer core radius is 325 km for GPM3, so $\Delta R = 155$ km and $V_{Slv}^2\, \partial k_2/\partial(V_{Slv}^2) = -0.00138$. The 6.9% difference of $k_2(P_F) - k_2(0) = 0.00157$ for GPM3 would require $\Delta V_{Slv}^2/V_{Slv}^2 = -1.1$, which is impossibly large, because it is out of the linear range of the partial derivative. With the larger radius for the low-velocity zone in Table 8 for GPM3, $\Delta R_{lv} = 209$ km and $\Delta V_{Slv}^2/V_{Slv}^2 = -0.8$, which is more acceptable, but this large change is still affected by nonlinearity in the partial derivative. The actual value used to construct the GPM models of Table 8 was $\Delta V_{Slv}^2/V_{Slv}^2 = -0.64$, so the second partial derivative must be positive. This exercise is predicated on the assumption that all of the power law dissipation is due to the low-velocity zone, but some must originate in shallower mantle layers, which would decrease the magnitude of ΔV_{Slv}.

Curves of $k_2(P)/Q(P)$ are illustrated in Figure 5. Periods span 1 day to 10^5 days. The GPM3 model is used as an example. Four curves are shown using the four pairs of w and ξ values tabulated in Table 10. Finite ξ values deflect the curves upward at long periods. The four model curves pass through the section 6 LLR value of $(k_2/Q)_F = (6.4 \pm 0.6) \times 10^{-4}$. The three dashed lines show the LLR results derived for k_2/Q versus period and the 1 standard deviation (±1σ) uncertainties for periods from 0.5 month to 6 years. The exponent that is fit in section 6 is $w = -0.17 \pm 0.10$. The figure also shows the separate 1 month and 1 year LLR determinations as circles with uncertainties. Those two points alone are compatible with a range of small positive or negative exponents. However, the determination of the 3 year dissipation term in Table 5 is incompatible with positive values of w, but it cannot be plotted as a separate determination, because it depends on k_2/Q values at 0.5 month, 1 month, and 3 years [*Williams et al.*, 2001]. Similarly, the 206 day term in Table 5 depends on k_2/Q values at 0.5 month, 1 month, and 206 days. A comparison of LLR results with model values in Figure 5 implies that the lunar k_2/Q curve is not as simple as either an anelastic power law or a power law plus viscosity. Although the power law seems to model the average change from seismic periods to tidal periods reasonably well, an inflection in the curve in the vicinity of tidal periods is suspected. Alternatively, there may be other influences on the out-of-phase physical libration components that are not well understood. The 1095 day term is close to a resonance at 1056 days that magnifies the importance of small influences. Although the large k_2/Q values in the upper right portion of the figure should be considered speculative, we chose to extend the curves through the period of the lunar analog of the Chandler wobble at 27,257 days = 74.6 years [*Rambaux and Williams*, 2011].

During the numerical integration of the lunar orbit and physical librations, a tidal time delay model is used rather than a series representation [*Standish and Williams*, 2012; *Folkner et al.*, 2014]. The time delay model gives dissipation that depends on the inverse period. It should represent the dissipation at 1 month, and the line in Figure 5 is shown passing through the DE430 monthly value of k_2/Q, but the time delay model does not represent the smaller contributions at other periods well. That difference motivates LLR data analysis to fit the terms in Table 5.

The model values of real k_2 and k_2/Q are illustrated in Figure 6 for the GPM3 model. The periods span 1 day to 10^5 days. At a 1 month period, the two sets of curves are constrained to the GRAIL-determined real k_2 and the LLR-derived k_2/Q, which are indicated with arrows. Compared with the monthly k_2, the predicted 0.5 month k_2 is only 1% smaller, the annual k_2 is 6% larger, and the 3 year value is 10% greater. For the anelastic case, the predicted 6 year k_2 is 13% larger, and the 74.6 year wobble value is 30% greater than the monthly k_2.

The amplitudes of the 0.5 month tides are 13–19% of the monthly amplitudes. With only a 1% difference expected for real k_2 at the two periods, it would be difficult to detect that frequency dependence. The sensitivity of physical librations to k_2 is strongest at monthly periods, whereas sensitivity at shorter or longer periods is weak.

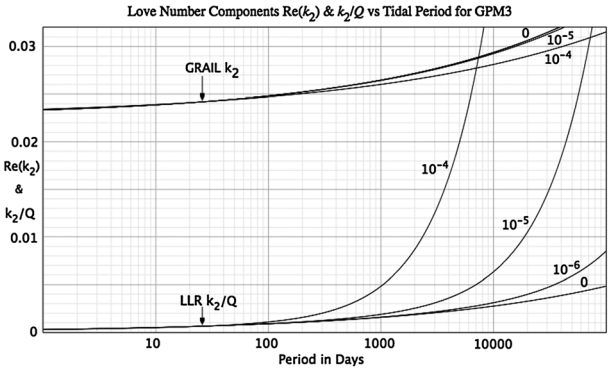

Figure 6. Model Love number components $k_{2r} = \mathrm{Re}(k_2)$ and k_2/Q versus period for the GPM3 model. The viscosity-related parameter ξ has model values of 0, 10^{-6}, 10^{-5}, and 10^{-4}.

The physical librations have three well-determined periods for resonances: 1056 days in longitude librations, plus 27.30 days and 74.6 years in latitude librations. [*Rambaux and Williams*, 2011]. The amplification of long-period librations by resonances allows LLR data analysis to extract the information on k_2/Q versus period that has been presented here.

The solutions in Table 10 can be extrapolated down to seismic periods. For the five anelastic values of w, the tidal Q at 1 s ranges from 5000 for $w = 0.34$ to 700 at $w = 0.20$. The Q_S for an S wave is twice the $Q(r)$ for $\mu(r)$, since V_S is proportional to $\mu^{1/2}$. *Nakamura and Koyama* [1982] found a Q_S value of several thousand in the upper mantle at ~5 Hz, but the Q_S decreases to ~1500 in the middle mantle [*Nakamura et al.*, 1976] and decreases further to <500 in the attenuating zone. Our tidal Q extrapolated to the seismic range with an anelastic power law cannot be compared directly with local values of Q_S without making assumptions about the distribution of dissipation. For dissipation concentrated in a low-velocity layer with an outer radius of 480 km [*Weber et al.*, 2011], the models give Q_S values at 1 s of ~400 for $w = 0.34$ and ~100 at $w = 0.20$, which are compatible with the seismic results. The inverse square root of equation (28) relates Q_S to dispersive S wave propagation for the combined Andrade and Maxwell model.

The measurement of free oscillations of the Moon would give important information about its interior structure and elastic properties. The gravest torsional mode has a predicted period of ~16 min, and other mantle modes would be shorter [*Gudkova and Zharkov*, 2002; *Gudkova and Raevskii*, 2013]. The tidal Q values extrapolated to an 8 min period for GPM models 1–5 are ~600–200, 8–3 times less than for seismic periods, respectively.

The GRAIL and LLR data analyses are sensitive to tidal variations through k_2. LLR also has some sensitivity to tidal displacements. The partial derivatives of the Love numbers in Table 11 show that k_2 and h_2 have similar sensitivities to layer μ values in a relative sense, but the sensitivity of l_2 to the deep mantle is much weaker. The Q values associated with k_2 and h_2 should be similar, but if the tidal Q is mainly coming from the low-velocity zone, then the Q for l_2 should be an order of magnitude larger. Dissipation in the upper mantle would decrease the Q associated with l_2. Tidal dissipation should affect the monthly vertical displacement at the Apollo 11 and 14 sites by about 2.5 mm. The effect on the horizontal tides should be on the order of 0.1 mm.

For the response of material to stress, *Efroimsky* [2012a, 2012b] employed a representation equivalent to equation (28) with combined Andrade and Maxwell influences. A body's phase-shifted response to tidal forcing is expressed by k_2/Q, but even for a homogeneous body, the tidal Q is not identical to the Q associated with μ. However, they would be similar for a homogeneous Moon so long as $19V_S^2/V_e^2 \approx 65$. At very long periods, k_2/Q is reduced by self-gravitation so as to cause a maximum in k_2/Q versus frequency. To explain the LLR results, Efroimsky exploited the interplay of rheology and gravity and proposed that the dissipation-related phase-shifted tidal response is near this maximum. To this end, he was led to propose a viscosity of $\sim 3 \times 10^{15}$ Pa s based on a homogeneous incompressible model for the Moon. The Maxwell relaxation time η/μ would then be ~0.5 day, which is much shorter than any model considered in this section. As illustrated by *Efroimsky* [2012b] for the homogeneous lunar model, both $Re(k_2)$ and k_2/Q approach 0.7 at long periods, k_2/Q has a maximum, and the curve turns over for longer periods. As the period approaches infinity, k_2/Q approaches 0, while k_2 approaches its fluid value. A large Love number is not observed for the Moon, but with a shift of frequency scale, this model predicts k_2 and k_2/Q over a very wide range of periods. A reversal of slope is not expected for equation (28) and is not predicted by equation (29); some modification, such as additional terms based on nonlinear partial derivatives, would be required to capture a turnover of k_2/Q.

Whereas *Efroimsky* [2012a, 2012b] considered that a zone of partial melting might be a source of viscous behavior, *Nimmo et al.* [2012] went further by suggesting that the attenuating layer is not a zone of partial

melting but rather a zone in which creep becomes important at tidal frequencies. Heat speeds up the creep, so the model has a hot deep mantle and core. Their baseline model has a temperature of 1410°C at the CMB, and the comments in the previous section on core temperature and density apply. Such a temperature would be more consistent with the cooling calculations by *Spohn et al.* [2001] than the model by *Ziethe et al.* [2009]. Despite the high temperature, flattening of the CMB does not necessarily relax. However, *Meyer and Wisdom* [2011] and *Le Bars et al.* [2011] demonstrated that CMB distortions of the size of *f* in Table 3 can be relaxed, shaped by a nonequilibrium mantle's internal potential, see the comments on Table 3 in section 5. The Nimmo et al. model gave a tidal *Q* similar to the LLR result, but it does not give the dependence on period that LLR indicates. The Nimmo et al. model predicts a 10% increase in k_2 when passing from the short-period elastic limit to a 1 month period, somewhat larger than the 5–9% increases in Table 10.

A small amount of water in the lunar interior would change its properties. *Karato* [2013] found that water lowers seismic and tidal *Q* and increases electrical conductivity. Defect-related processes are affected by water content and temperature. Mantle temperatures can be cooler than those required for a partial melt or creep. The lower mantle zone of low *Q* appears to be thicker for the creep and water processes than for a partial melt, so that the material of the zone can have larger *Q*. Karato suggested that tidal strain may be nonlinear, but the strain value that was given was an order of magnitude too large.

The Moon has a low-velocity zone, but the reduction in velocity and attenuation in the zone are different for seismic and tidal periods. Changes in the Love numbers with period are related to the variation of dissipation with period. Lunar viscoelastic models are constructed by combining seismic data at short periods with the GRAIL-derived k_2 and LLR-determined k_2/Q at tidal periods. Frequency-dependent models are needed to fully exploit the 1% accuracy of the GRAIL analysis. It is important to test the variation of k_2 and k_2/Q as functions of period with very accurate observations and analyses.

9. Future Possibilities

The results of this paper are based on the analysis of the GRAIL Primary Mission data. The data analysis models are still improving, and that progress should lead to improved fits [*Konopliv et al.*, 2013; *Lemoine et al.*, 2013]. The GRAIL Extended Mission obtained lower altitude data suitable for a high-resolution gravity field. Higher-degree fields are being fit to the combined Primary and Extended Mission data [*Goossens et al.*, 2014; *Konopliv et al.*, 2014]. We anticipate some improvement in the Love number and low-degree field from analyzing the two blocks of data jointly.

Lunar laser ranging analysis (section 6) yields a monthly tidal *Q* of about 37.5 ± 4. Future GRAIL data analysis may be able to detect tidal dissipation as an ~1.5° phase shift in the largest monthly tidal variations. Given tidal dissipation, both k_2 and k_2/Q are expected to vary with period, possible future subjects for investigation.

Zhong et al. [2012] suggested that there may be a small nonspherical response to tidal forcing due to asymmetric elastic properties between the lunar nearside and farside. They proposed that this asymmetry would change the degree-2 tides and introduce a mixed-mode degree-3 response. Future GRAIL data analysis can search for these effects.

The inner core could be slightly oblate from spin and triaxial from tides. Both spin and tides would have been stronger, when the early Moon was closer to Earth. Compared with a current equilibrium shape, which the whole Moon does not exhibit, an order of magnitude larger equilibrium shape would result for the Moon early in its evolution. But there are questions of relaxation for the hot deep mantle, CMB, and inner core. The shape of the CMB may be a local equilibrium shape controlled by the interior gravity field of the mantle [*Meyer and Wisdom*, 2011; *Le Bars et al.*, 2011]. GRAIL data analysis may detect an inner core through its gravity field, a possibility that was proposed by *Williams* [2007]. Although inner core rotation is expected to be synchronous on average, small oscillations in orientation would not precisely follow that of the mantle. In particular, the two poles of rotation would not be expected to line up. Thus, any nonspherical gravity field of the inner core would cause a variable gravity component when measured in the frame of the crust and mantle. Analysis of GRAIL data to search for such a variable component is warranted.

GRAIL data analysis has not yet exhausted the information content of the data. The view of the lunar tidal response is evolving from simpler models to more complex possibilities. Also, an inner core gravity field may

reveal its presence through variable C_{21} and S_{21} coefficients. There are a number of future possibilities for GRAIL data analysis and interior results.

Future missions to the Moon will benefit from GRAIL data analysis results. Important studies of complementary data sets can be conducted by orbiting or landed spacecraft, and indeed the GRAIL gravity field will improve the precision of future landings. Such missions will be opportunities to learn more about the lunar interior.

10. Summary

GRAIL data analysis has produced a high-resolution map of the lunar gravity field [*Zuber et al.*, 2013b]. This paper is concerned with the interior-related lunar properties: mean density, moment of inertia of the solid Moon, elastic tidal response specified by the potential Love number k_2, and tidal dissipation. Lunar structure includes a thin crust, a deep mantle, a fluid outer core, and a suspected solid inner core. A layer of low shear wave velocity and enhanced attenuation is thought to lie just above the outer core. An accurate Love number is sensitive to the fluid core size as well as the size and *S* wave velocity in the attenuating layer. Interior models are fit to density, moment, k_2, and tidal dissipation k_2/Q. A summary follows.

The GRAIL Primary Mission (PM) lasted for 3 months with data from 1 March to 29 May 2012. The PM was designed to have only one major orbit maneuver in order to change the mutual drift rate of the two spacecraft from separating to closing. The two long, low-activity intervals are ideal for determining properties of interest for the lunar interior, including tidal response and low-degree gravity field. This paper uses solutions for these parameters from the PM data. Solutions from two independent analysis programs and groups [*Konopliv et al.*, 2013; *Lemoine et al.*, 2013] provide a cross check.

GRAIL has improved the lunar-orbiting spacecraft *GM*, but the Table 1 value of $4902.80007 \pm 0.00014\ \mathrm{km^3/s^2}$, from the joint lunar and planetary ephemeris fit leading to DE430, has smaller uncertainty. The lunar mass *M* given in section 2 is $(7.34630 \pm 0.00088) \times 10^{22}$ kg, and the mean density is $3345.56 \pm 0.40\ \mathrm{kg/m^3}$ for the mean radius of 1737.151 km. The 0.012% uncertainty in the gravitational constant *G* so dominates the uncertainty for the lunar mass and mean density that all modern values of lunar *GM* in Table 1 give compatible results for mass and density.

Theoretical expressions for the moments of inertia are reviewed in section 3. The principal moments of the whole Moon are *A*, *B*, and *C*, ordered by increasing size. Moments result from combinations of spacecraft-determined J_2 and C_{22} with lunar laser ranging (LLR) determinations of orientation-related $\gamma = (B - A)/C$ and $\beta = (C - A)/B$.

Tide and physical libration models are described in section 4. Expressions are given for the tidal variations of the potential and the moment of inertia matrix. The constant part of the degree-2 tidal potential is added to the spacecraft solution parameters for J_2 and C_{22}. Analogous corrections to β and γ are also made, and the whole-Moon moments of inertia are calculated. The three-dimensional orientation, or physical libration, is sensitive to $(B - A)/C_s$ and $(C - A)/B_s$, where the subscript *s* stands for the solid crust, mantle, and inner core of the Moon without the fluid core. The moments A_s, B_s, and C_s are derived more accurately than *A*, *B*, and *C*. Consequently, the fluid core moments of the physical libration model are subtracted from the *A*, *B*, and *C* to obtain A_s, B_s, and C_s.

New fits of lunar laser ranges and planetary-tracking data led to a simultaneous integration of the lunar and planetary orbits and lunar physical librations. The iterated fits and integrations used the GRAIL-derived Love number and low-degree gravity field coefficients. This step assured compatibility between the strongly improved GRAIL field and the lunar laser physical libration parameters. A selected set of lunar parameter values is given in Table 3 of section 5. The new ephemeris, designated DE430, is available to the public [*Williams et al.*, 2013; *Folkner et al.*, 2014].

The best estimate for the mean moment of inertia of the solid Moon, the crust, the mantle, and any inner core given in section 5 is $I_s/MR^2 = 0.392728 \pm 0.000012$ for a gravity reference radius $R = 1738$ km or $I_s/MR^2 = 0.393112 \pm 0.000012$ for a mean radius $R = 1737.151$ km. The MR^2 product makes the normalized ratio dimensionless. This moment results from combining two independent GRAIL determinations of the degree-2 gravity field with a lunar laser ranging determination of the β and γ values, see Tables 3 and 4 in section 5. The gravity coefficients and mean moment are strongly improved by GRAIL. A uniform-density Moon would have a normalized moment of 0.4, so the influence of structure is subtle.

The GRAIL-determined value for the k_2 Love number is 0.02416 ± 0.00022, with $R = 1738$ km, and 0.02422 ± 0.00022, for $R = 1737.151$ km. This value is the average of two independent analyses of data, see Table 4 and section 5. A selective average of several pre-GRAIL spacecraft and lunar laser determinations of Love number k_2 gives 0.0245 ± 0.0012, see the Appendix. GRAIL has reduced the uncertainty from 5% to 1%. Attesting to GRAIL's sensitivity, the detection of the third-degree Love number is an impressive accomplishment. Sensitivity to higher-degree Love numbers falls off by 2 orders of magnitude per degree, so accurate higher-degree Love numbers are not expected from GRAIL.

Dissipation in the Moon introduces phase shifts in the tidal response. Effects of dissipation have been determined by lunar laser ranging (LLR) and are updated in section 6. Subject to the assumption of a power law dependence of k_2/Q with tidal period, a solution for DE430 leads to a monthly k_2/Q of $(6.4 \pm 0.6) \times 10^{-4}$ and, using the GRAIL k_2, a monthly Q of 37.5 ± 4. LLR analysis obtains a decrease of k_2/Q with increasing tidal period rather than the expected increase. The monthly k_2/Q amounts to $2.7 \pm 0.3\%$ of the GRAIL-determined k_2, a phase shift of $1.5° \pm 0.2°$.

Section 7 concerns lunar interior models. The GRAIL-derived moment and k_2, suitable for the mean topographic radius, are compared with two published models of the lunar interior in Tables 6 and 7. With the assumptions that an inner core has the density of iron, the outer core is near the density of the Fe-FeS eutectic composition, and mantle and crustal densities are fixed, the mean density and moment set limits to the radii for the inner and outer core.

Moment, density, and Love number are matched by a sequence of models that vary the outer radii of the inner and outer core and of the deep mantle low-velocity layer but hold densities of structures fixed. Structural and Love number information are presented for five GPM models in Table 8. Figures 1–3 show their core radii, mass fractions, and moment of inertia fractions, respectively, and Figure 4 profiles density and seismic velocities for one model. If the density of the outer core is increased or the density of the crust is decreased, the limiting radii shift as shown in Table 9. The mass of the crust is a major uncertainty. For the spread of models generated to fit the new results we find the following: A plausible range for the fluid outer core radius is about 200–380 km, giving a global mass fraction of 0–1.5%. The inner core has a radius of approximately 0–280 km and a mass fraction of 0–1%. The combined inner and outer core mass fraction is ≤1.5%.

The Love number is most sensitive to outer core radius and mantle S wave velocity. The upper mantle was probed by the Apollo seismic experiment, and the outer core radius is constrained by the mean density and moment. Consequently, an accurate Love number illuminates a combination of the extent of and decrease in lower mantle S wave velocity. Dissipation has been detected at both seismic and tidal periods, but with different values for Q. Section 8 explores how dissipation causes the Love numbers and k_2/Q to vary with period. Viscoelastic model parameters are presented in Table 10 for the five GPM models; the parameters connect the behavior between seismic and tidal periods. Although tidal dissipation in the Moon has a smaller Q than tidal Q for the solid Earth, the derived exponents for frequency dependence are comparable with values from laboratory and terrestrial experience. To exploit the full accuracy of the tidal and seismic data, the influence of dissipation on the Love number must be taken into account. Frequency-dependent damping also affects free oscillations and free librations.

What are the future possibilities for GRAIL data analysis? (1) We anticipate improved accuracy for the data analysis results from the GRAIL PM. (2) Detection of the monthly tidal dissipation is a future possibility for GRAIL. (3) Asymmetries in the Moon's elastic properties would complicate the tidal response [*Zhong et al.*, 2012]. (4) Tidal Love numbers should depend on frequency. (5) An inner core would produce a time-varying signal in the gravity field [*Williams*, 2007]. The signal is expected to be weak however, and it is unclear whether its strength will exceed GRAIL's threshold. Future GRAIL analyses can refine results from the Primary Mission and explore new effects.

GRAIL analysis has yielded a lunar gravity field with unprecedented accuracy. Ongoing data analysis is extracting improving results on the static and time-varying gravity field. This information is increasing our knowledge of the Moon and its interior properties.

Appendix A: Interior Properties Prior to GRAIL

In this appendix, we present two LLR solutions, three sets of spacecraft-determined J_2 and C_{22} values, 12 resulting derivations of the mean moment of inertia, and eight k_2 values from the last 1.5 decades. These

Table A1. Two Pre-GRAIL LLR Solutions With Two Different Fixed Fluid Core Moments

Parameter	LLR3	LLR7
β	$(631.320 \pm 0.080) \times 10^{-6}$	$(631.059 \pm 0.081) \times 10^{-6}$
γ	$(227.826 \pm 0.006) \times 10^{-6}$	$(227.735 \pm 0.006) \times 10^{-6}$
J_{2tr}	$(203.70 \pm 0.41) \times 10^{-6}$	$(203.51 \pm 0.42) \times 10^{-6}$
k_2	0.0247 ± 0.0016	0.0235 ± 0.0019
h_2	0.045 ± 0.008	0.045 ± 0.008
l_2	0.0107	0.0107
C_f/C	3×10^{-4}	7×10^{-4}
K/C	$(1.39 \pm 0.15) \times 10^{-8}\,\mathrm{d}^{-1}$	$(1.52 \pm 0.14) \times 10^{-8}\,\mathrm{d}^{-1}$
f	$(4.7 \pm 1.7) \times 10^{-4}$	$(2.7 \pm 0.9) \times 10^{-4}$
$[C_f - (A_f + B_f)/2]/C$	$(1.4 \pm 0.5) \times 10^{-7}$	$(1.9 \pm 0.6) \times 10^{-7}$

results make use of pre-GRAIL information. These pre-GRAIL computations can be compared with the GRAIL results in section 5 to show the improvement.

The size and moment of the fluid outer core are uncertain. Consequently, Table A1 gives two parallel pre-GRAIL LLR solutions using two different outer core moment ratios C_f/C: 3×10^{-4} and 7×10^{-4}. The solutions are designated LLR3 and LLR7, respectively. They used 17,549 ranges from March 1970 to June 2011. The uncertainties for the β, γ, J_{2tr}, k_2, and h_2 parameters in the table do not include a contribution from the unknown C_f/C ratio. The difference in the two parallel solutions shows the systematic shift in the solution parameter values as the outer fluid core moment varies over a plausible spread of values. Those differences can be used to judge the additional uncertainties due to the C_f/C ratio. The last three parameters of Table 3 include a contribution from the C_f/C ratio as judged from their differences in Table A1. The LLR J_2 value is not used to derive moments in this appendix, but it may be compared with the more accurate spacecraft results. LLR is also sensitive to the displacement Love numbers h_2 and l_2, but the two second-degree displacement Love numbers are correlated and do not separate well in solutions. For the solutions given in the table, the displacement Love number l_2 was set to a model value of 0.0107, whereas both solutions gave $h_2 = 0.045 \pm 0.008$. Love number k_2 is better determined than h_2.

The 12 solid moment of inertia I_s/MR^2 values in Table A2 are derived from three pre-GRAIL spacecraft-determined pairs of J_2 and C_{22} coefficients combined with the two Table A1 LLR values of β and γ. The final moments include the constant part of the tidal distortion, the permanent tide. During the combination, individual LLR and spacecraft permanent tide corrections take account of their different k_2 values. The LP150Q solution has tracking data up through the Lunar Prospector mission. The two SGM fields also include SELENE tracking data, and the SGM100i solution adds SELENE VLBI data (see Table 1). In all three cases, J_2 gives a smaller uncertainty for the moment than C_{22} does. Also, for all the three cases, the moment derived from C_{22} comes out slightly smaller than the one from J_2. For the two SGM cases, the differences between the moments derived from J_2 and C_{22} are larger than the uncertainties. The uncertainties given for the LP150Q gravity coefficients are 10 times the formal uncertainties. For the two SGM cases, a factor of 20 times formal uncertainty is used for J_2 and C_{22}, but that adjustment does not cover the differences between the results. Considering the six moment values and their scatter, we suggest that $I_s/MR^2 = 0.3930 \pm 0.0003$ for $R = 1738$ km. The moment differences are known with much better accuracy; including the permanent tide, the moment differences are $(A_s - I_s)/MR^2 = -1.127 \times 10^{-4}$, $(B_s - I_s)/MR^2 = -0.229 \times 10^{-4}$, and $(C_s - I_s)/MR^2 = 1.356 \times 10^{-4}$, with the six spacecraft/LLR combinations differing by ≤2 in the last digit. For $R = 1737.151$ km, the $I_s/MR^2 = 0.3934 \pm 0.0003$.

Table A2. Three Pre-GRAIL Spacecraft Results for Love Number k_2, Unnormalized J_2 and C_{22} Gravity Coefficients, and Moments of Inertia Derived by Combining With LLR β and γ

Parameter	LP150Q	SGM100h	SGM100i
R	1738.0 km	1738.0 km	1738.0 km
k_2	0.0248 ± 0.0030	0.0240 ± 0.0015	0.0255 ± 0.0016
J_{2tr}	$(203.261 \pm 0.120) \times 10^{-6}$	$(203.450 \pm 0.074) \times 10^{-6}$	$(203.475 \pm 0.074) \times 10^{-6}$
C_{22tr}	$(22.358 \pm 0.024) \times 10^{-6}$	$(22.372 \pm 0.016) \times 10^{-6}$	$(22.370 \pm 0.012) \times 10^{-6}$
J_{2p}	$(203.353 \pm 0.121) \times 10^{-6}$	$(203.539 \pm 0.074) \times 10^{-6}$	$(203.570 \pm 0.074) \times 10^{-6}$
C_{22p}	$(22.404 \pm 0.025) \times 10^{-6}$	$(22.417 \pm 0.016) \times 10^{-6}$	$(22.417 \pm 0.012) \times 10^{-6}$
J_{2p} + LLR3 → I_s/MR^2	0.39279 ± 0.00024	0.39314 ± 0.00018	0.39320 ± 0.00018
J_{2p} + LLR7 → I_s/MR^2	0.39280 ± 0.00024	0.39316 ± 0.00018	0.39322 ± 0.00018
C_{22p} + LLR3 → I_s/MR^2	0.39230 ± 0.00044	0.39252 ± 0.00028	0.39252 ± 0.00022
C_{22p} + LLR7 → I_s/MR^2	0.39234 ± 0.00044	0.39256 ± 0.00028	0.39256 ± 0.00022

Table A3. Recent Pre-GRAIL Love Number k_2 Determinations

ID	k_2	Data Sets[a]	Citation
LP165P	0.026 ± 0.003	LO to LP tracking	*Konopliv et al.* [2001]
LP150Q	0.0248 ± 0.003	LO to LP tracking	*Konopliv* [2000]
-	0.0213 ± 0.0075	LO to LP tracking	*Goossens and Matsumoto* [2008]
SGM100h	0.0240 ± 0.0015	LO to SELENE tracking	*Matsumoto et al.* [2010]
SGM100i	0.0255 ± 0.0016	LO to SELENE tracking + VLBI	*Goossens et al.* [2011a]
SGM150j	0.0252 ± 0.0010	LO to SELENE tracking + VLBI + LP XM	*Goossens et al.* [2011b]
LLR3	0.0247 ± 0.0016	LLR 1970–2011	This paper
LLR7	0.0235 ± 0.0019	LLR 1970–2011	This paper

[a]LO = Lunar Orbiter, LP = Lunar Prospector, and XM = Extended Mission.

Mazarico et al. [2010] analyzed tracking data from the NASA's Lunar Orbiter to Lunar Prospector spacecraft. The Love number was fixed while deriving the GLGM-3 gravity field. A recent gravity field solution called LPE200 was derived from an analysis of Lunar Prospector tracking data [*Han et al.*, 2011]. The low-degree gravity coefficients from GLGM-3 were adopted for the LPE200 field. The J_2 and C_{22} coefficients give moments of inertia that are almost identical to the corresponding LP150Q moments. The GLGM-3 and LPE200 moments are not listed in Table A2. The LP150Q gravity field used a different data analysis program than the GLGM-3, LPE200, and the three SGM fields.

Compared with the pre-GRAIL knowledge of the lunar moments of inertia and their differences, GRAIL improves the J_2 and C_{22} uncertainties by a large amount and reduces the uncertainties in the moments. Less apparently, the pre-GRAIL LLR β and γ uncertainties were limited by the gravity field uncertainties, most strongly by C_{31} and C_{33}, and reprocessing the LLR data with an improved gravity field improves β, γ, the orbit, and physical librations. Table 4, compared with Table A2, shows an order of magnitude improvement in the moments of the solid Moon from GRAIL.

A summary of recent pre-GRAIL orbiting spacecraft and LLR determinations of the lunar potential Love number k_2 is given in Table A3. The spacecraft analyses include gravity field as well as tidal Love number. The spacecraft determinations of k_2 are sensing tidal variations of the gravity field. The mission data sets in the determinations are described in section 2.

The lunar laser ranging (LLR) determinations of Love number k_2 are sensitive to data span and choice of solution parameters. The flattening f of the outer core is anticorrelated with both k_2 and the fluid core moment of inertia. Independent of LLR, there is no determination of flattening f.

For each spacecraft-determined gravity field, the simultaneously determined Love number k_2 should be used with the second-degree coefficients. An average k_2 value should be more accurate than individual determinations. An equally weighted average of the LP150Q, SGM100h, SGM100i, and two LLR values gives $k_2 = 0.0245$. The uncertainties in the spacecraft-determined values are not independent, because the data sets overlap in part. Considering the spread of the five values and overlapping data sets, we adopt a pre-GRAIL uncertainty of ±0.0012 or 5%, so $k_2 = 0.0245 \pm 0.0012$. GRAIL analysis determines the Love number with a 1% uncertainty (see Table 4 in section 5), a factor of 5 improvement over pre-GRAIL knowledge.

Notation

A Smallest principal moment of inertia
a Largest CMB equatorial radius
B Second principal moment of inertia
b Smallest CMB equatorial radius or dissipation coefficient
C Largest principal moment of inertia
c Polar CMB radius.
C_{22} Degree-2 gravitational field coefficient
D Elongation of Moon from Sun
f Flattening of the outer core
F Lunar argument of latitude
G Gravitational constant, $m^3/kg\,s^2$

h_2	Degree-2 vertical displacement Love number
h_{2f}	Degree-2 vertical displacement fluid Love number
i	$\sqrt{(-1)}$
I	Inclination of lunar equator plane to ecliptic plane
I_f	Mean moment of inertia of fluid outer core
I_i	Mean moment of inertia of solid inner core
I_m	Mean moment of inertia $(A+B+C)/3$
$\mathbf{I}_{pt}$	Permanent tide moment of inertia matrix
I_s	Mean moment of inertia of solid Moon, $(A_s+B_s+C_s)/3$
$\mathbf{I}_{tr}$	Tide-removed moment of inertia matrix
$\mathbf{I}_{vt}$	Variable tide moment of inertia matrix
$\mathbf{I}_{vs}$	Variable spin moment of inertia matrix
J_2	Degree-2 gravitational field coefficient
k_2	Degree-2 potential Love number
k_{2f}	Degree-2 potential fluid Love number
K	Dissipation coefficient
K_S	Adiabatic bulk modulus
l	Lunar mean anomaly
l'	Solar or Earth-Moon center of mass mean anomaly
l_2	Degree-2 horizontal displacement Love number
l_{2f}	Degree-2 horizontal displacement fluid Love number
M	Mass
M_f	Mass of fluid outer core
M_i	Mass of solid inner core
P	Period
P_F	27.212 day period of argument of latitude
Q	Quality factor for dissipation
R	Reference radius, km
R_f	Radius of fluid outer core, km
R_i	Radius of solid inner core, km
R_{lv}	Radius of low velocity layer, km
r	Radial distance
t	Time
V_e	Escape velocity
V_P	Seismic *P* wave velocity
V_S	Seismic *S* wave velocity
V_{2p}	Tidal potential
w	Exponent in power law representation of dissipation
α	Physical libration parameter $(C-B)/A$
β	Physical libration parameter $(C-A)/B$
γ	Physical libration parameter $(B-A)/C$
Δ	Small change
η	Shear viscosity
μ	Shear modulus
ξ	Coefficient related to inverse viscosity
ρ	Density or component of physical libration in latitude
ρ_m	Mean density, kg/m^3
σ	Component of physical libration in latitude
τ	Physical libration in longitude
ω	Angular rate vector

Subscripts

f	Fluid or fluid outer core
F	Argument of latitude

i	Solid inner core
j	Index for layers
lv	Low velocity
m	Mean
p	Permanent or external body (Earth or Sun)
P	*P* wave
pt	Permanent tide
s	Solid Moon
S	*S* wave
t	Tide
tr	Tide removed
vs	Variable spin
vt	Variable tide

Abbreviations

CMB	core-mantle boundary
GL	GRAIL Lunar
GLGM	Goddard Lunar Gravity Model
GLTM	Goddard Lunar Topography Model
GPM	GRAIL Primary Mission
GRAIL	Gravity Recovery and Interior Laboratory
GRGM	GRAIL Gravity Model
GSFC	Goddard Space Flight Center
JPL	Jet Propulsion Laboratory
LLR	lunar laser ranging
LO	Lunar Orbiter
LOLA	Lunar Orbiter Laser Altimeter
LP	Lunar Prospector
LRO	Lunar Reconnaissance Orbiter
PDS	Planetary Data System
PM	Primary Mission
PRIM	Primary Mission
SELENE	Selenological and Engineering Explorer
SGM	SELENE Gravity Model
XM	Extended Mission

Acknowledgments

M. Efroimsky commented on tides and dissipation. K. Matsumoto and S.-C. Han provided information on their separate solutions. The GRAIL mission is a component of the NASA Discovery Program under contract to the Massachusetts Institute of Technology. The lunar laser ranging efforts at the McDonald Observatory, Observatoire de la Côte d'Azur, and Apache Point Observatory provided data that are archived by the International Laser Ranging Service at http://www.iers.org/IERS/EN/Organization/TechniqueCentres/ILRS/ilrs.html. A portion of the research described in this paper was carried out at the Jet Propulsion Laboratory of the California Institute of Technology, under a contract with the National Aeronautics and Space Administration.

References

Andrews-Hanna, J. C., et al. (2013), Ancient igneous intrusions and the early expansion of the Moon revealed by GRAIL gravity gradiometry, *Science*, *339*, 675–678, doi:10.1126/science.1231753.

Araki, H., et al. (2009), Lunar global shape and polar topography derived from Kaguya-LALT laser altimetry, *Science*, *323*, 897–900, doi:10.1126/science.1164146.

Asmar, S. W., et al. (2013), The scientific measurement system of the Gravity Recovery and Interior Laboratory (GRAIL) mission, *Space Sci. Rev.*, *178*, 25–55, doi:10.1007/s11214-013-9962-0.

Bills, B. G. (1995), Discrepant estimates of moments of inertia of the Moon, *J. Geophys. Res.*, *100*, 26,297–26,303, doi:10.1029/95JE03100.

Brett, R. (1973), A lunar core of Fe-Ni-S, *Geochim. Cosmochim. Acta*, *37*, 165–170, doi:10.1016/0016-7037(73)90255-X.

Brett, R., and P. M. Bell (1969), Melting relations in the Fe-rich portion of the system Fe-FeS at 30 kb pressure, *Earth Planet. Sci. Lett.*, *6*, 479–482, doi:10.1016/0012-821X(69)90119-8.

Chen, B., J. Li, and S. A. Hauck II (2008), Non-ideal liquidus curve in the Fe-S system and Mercury's snowing core, *Geophys. Res. Lett.*, *35*, L07201, doi:10.1029/2008GL033311.

Dickey, J. O., et al. (1994), Lunar Laser Ranging: A continuing legacy of the Apollo program, *Science*, *265*, 482–490, doi:10.1126/science.265.5171.482.

Dunn, P., M. Torrence, R. Kolenkiewicz, and D. Smith (1999), Earth scale defined by modern satellite ranging observations, *Geophys. Res. Lett.*, *26*, 1489–1492, doi:10.1029/1999GL900260.

Dwyer, C. A., D. J. Stevenson, and F. Nimmo (2011), A long-lived lunar dynamo driven by continuous mechanical stirring, *Nature*, *479*, 212–214, doi:10.1038/nature10564.

Eckhardt, D. H. (1973), Physical librations due to the third and fourth degree harmonics of the lunar gravity potential, *Moon*, *6*, 127–134, doi:10.1007/BF02630658.

Efroimsky, M. (2012a), Tidal dissipation compared to seismic dissipation: In small bodies, earths, and super-earths, *Astrophys. J.*, *746*, 150, doi:10.1088/0004-637X/746/2/150. Erratum (2013), *Astrophys. J.*, *763*, 150, doi:10.1088/0004-637X/763/2/150.

Efroimsky, M. (2012b), Bodily tides near spin orbit resonances, *Celest. Mech. Dyn. Astron.*, *112*, 283–330, doi:10.1007/s10569-011-9397-4.
Ferrari, A. J., W. S. Sinclair, W. L. Sjogren, J. G. Williams, and C. F. Yoder (1980), Geophysical parameters of the Earth-Moon system, *J. Geophys. Res.*, *85*, 3939–3951, doi:10.1029/JB085IB07p03939.
Fok, H. S., et al. (2011), Accuracy assessment of lunar topography models, *Earth Planets Space*, *63*, 15–23, doi:10.5047/eps.2010.08.005.
Folkner, W. M., J. G. Williams, and D. H. Boggs (2008), The planetary and lunar ephemeris DE 421, IOM 343R-08-003, Jet Propul. Lab., Pasadena, Calif., 31 March.
Folkner, W. M., J. G. Williams, D. H. Boggs, R. S. Park, and P. Kuchynka (2014), The planetary and lunar ephemerides DE430 and DE431, *Interplanetary Network Progress Rep. 42–196*, Jet Propul. Lab., Pasadena, Calif., 15 Feb.
Garcia, R. F., J. Gagnepain-Beyneix, S. Chevrot, and P. Lognonne (2011), Very preliminary reference Moon model, *Phys. Earth Planet. Inter.*, *188*, 96–113, doi:10.1016/j.pepi.2011.06.015.
Garrick-Bethell, I., B. P. Weiss, D. L. Shuster, and J. Buz (2009), Early lunar magnetism, *Science*, *323*, 356–359, doi:10.1126/science.1166804.
Goins, N. R., A. M. Dainty, and M. N. Toksöz (1981), Lunar seismology: The internal structure of the Moon, *J. Geophys. Res.*, *86*, 5061–5074, doi:10.1029/JB086IB06p05061.
Goldreich, P. (1967), Precession of the Moon's core, *J. Geophys. Res.*, *72*, 3135–3137, doi:10.1029/JZ072I012p03135.
Goldstein, B. E., R. J. Phillips, and C. T. Russell (1976), Magnetic permeability measurements and a lunar core, *Geophys. Res. Lett.*, *3*, 289–292, doi:10.1029/GL003I006p00289.
Goossens, S., and K. Matsumoto (2008), Lunar degree 2 potential Love number determination from satellite tracking data, *Geophys. Res. Lett.*, *35*, L02204, doi:10.1029/2007GL031960.
Goossens, S., et al. (2011a), Lunar gravity field determination using SELENE same-beam differential VLBI tracking data, *J. Geod.*, *85*, 205–228, doi:10.1007/s00190-010-0430-2.
Goossens, S., et al. (2011b), Improved high-resolution lunar gravity field model from SELENE and historical tracking data, Abstract P44B-05 presented at 2011 Fall Meeting, AGU, San Francisco, Calif., 5–9 Dec.
Goossens, S., et al. (2014), Global gravity field models of the Moon using GRAIL primary and extended mission data, *Lunar Planet. Sci.*, *45*, abstract 1619.
Gribb, T. T., and R. F. Cooper (1998), Low frequency shear attenuation in polycrystalline olivine: Grain boundary diffusion and the physical significance of the Andrade model for viscoelastic rheology, *J. Geophys. Res.*, *103*, 27,267–27,279, doi:10.1029/98JB02786.
Gudkova, T. V., and S. N. Raevskii (2013), Spectrum of the free oscillations of the Moon, *Sol. Syst. Res.*, *47*, 11–19, doi:10.1134/S0038094613010024.
Gudkova, T. V., and V. N. Zharkov (2002), The exploration of the lunar interior using torsional oscillations, *Planet. Space Sci.*, *50*, 1037–1048, doi:10.1016/S0032-0633(02)00070-3.
Han, S.-C., E. Mazarico, D. Rowlands, F. Lemoine, and S. Goossens (2011), New analysis of Lunar Prospector radio tracking data brings the nearside gravity field of the Moon with an unprecedented resolution, *Icarus*, *215*, 455–459, doi:10.1016/j.icarus.2011.07.020.
Hirayama, Y., T. Fujii, and K. Kurita (1993), The melting relation of the system, iron and carbon at high pressure and its bearing on the early stage of the Earth, *Geophys. Res. Lett.*, *20*, 2095–2098, doi:10.1029/93GL02131.
Hood, L. L., D. L. Mitchell, R. P. Lin, M. H. Acuña, and A. B. Binder (1999), Initial measurements of the lunar induced magnetic dipole moment using Lunar Prospector magnetometer data, *Geophys. Res. Lett.*, *26*, 2327–2330, doi:10.1029/1999GL900487.
Jackson, I., and U. H. Faul (2010), Grainsize-sensitive viscoelastic relaxation in olivine: Towards a robust laboratory-based model for seismological application, *Phys. Earth Planet. Inter.*, *183*, 151–163, doi:10.1016/j.pepi.2010.09.005.
Karato, S. (2013), Geophysical constraints on the water content of the lunar mantle and its implications for the origin of the Moon, *Earth Planet. Sci. Lett.*, *384*, 144–153, doi:10.1016/j.epsl.2013.10.001.
Kaula, W. M., and P. A. Baxa (1973), The physical librations of the Moon, including higher harmonic effects, *Moon*, *8*, 287–307, doi:10.1007/BF00581725.
Khan, A., K. Mosegaard, J. G. Williams, and P. Lognonné (2004), Does the Moon possess a molten core? — Probing the deep lunar interior using results from LLR and Lunar Prospector, *J. Geophys. Res.*, *109*, E09007, doi:10.1029/2004JE002294.
Klipstein, W. M., B. W. Arnold, D. G. Enzer, A. A. Ruiz, J. Y. Tien, R. T. Wang, and C. E. Dunn (2013), The lunar gravity ranging system for the Gravity Recovery and Interior Laboratory (GRAIL) mission, *Space Sci. Rev.*, *178*, 57–76, doi:10.1007/s11214-013-9973-x.
Konopliv, A. S. (2000), LP150Q file, submitted to PDS website on 27 November. [Available at http://pds-geosciences.wustl.edu/lunar/lp-l-rss-5-gravity-v1/lp_1001/sha/jgl150q1.lbl.]
Konopliv, A. S., A. B. Binder, L. L. Hood, A. B. Kucinskas, W. L. Sjogren, and J. G. Williams (1998), Improved gravity field of the Moon from Lunar Prospector, *Science*, *281*, 1476–1480, doi:10.1126/science.281.5382.1476.
Konopliv, A. S., S. W. Asmar, E. Carranza, W. L. Sjogren, and D.-N. Yuan (2001), Recent gravity models as a result of the Lunar Prospector mission, *Icarus*, *150*, 1–18, doi:10.1006/icar.2000.6573.
Konopliv, A. S., et al. (2013), The JPL lunar gravity field to spherical harmonic degree 660 from the GRAIL primary mission, *J. Geophys. Res. Planets*, *118*, 1415–1434, doi:10.1002/jgre.20097.
Konopliv, A. S., et al. (2014), High-resolution lunar gravity fields from the GRAIL Primary and Extended Missions, *Geophys. Res. Lett.*, *41*, 1452–1458, doi:10.1002/2013GL059066.
Le Bars, M., M. A. Wieczorek, Ö. Karatekin, D. Cébron, and M. Laneuville (2011), An impact-driven dynamo for the early Moon, *Nature*, *479*, 215–218, doi:10.1038/nature10565.
Lemoine, F. G., et al. (2013), High-degree gravity models from GRAIL primary mission data, *J. Geophys. Res. Planets*, *118*, 1676–1698, doi:10.1002/jgre.20118.
Matsumoto, K., et al. (2010), An improved lunar gravity field model from SELENE and historical tracking data: Revealing the farside gravity features, *J. Geophys. Res.*, *115*, E06007, doi:10.1029/2009JE003499.
Matsuyama, I. (2013), Fossil figure contribution to the lunar figure, *Icarus*, *222*, 411–414, doi:10.1016/j.icarus.2012.10.025.
Mazarico, E., F. G. Lemoine, S.-C. Han, and D. E. Smith (2010), GLGM-3: A degree 150 lunar gravity model from the historical tracking data of NASA Moon orbiters, *J. Geophys. Res.*, *115*, E05001, doi:10.1029/2009JE003472.
Melosh, H. J., et al. (2013), The origin of lunar mascon basins, *Science*, *340*, 1552–1555, doi:10.1126/science.1235768.
Meyer, J., and J. Wisdom (2011), Precession of the lunar core, *Icarus*, *211*, 921–924, doi:10.1016/j.icarus.2010.09.016.
Mohr, P. J., B. N. Taylor, and D. B. Newell (2012), CODATA recommended values of the fundamental physical constants: 2010, *Rev. Mod. Phys.*, *84*, 1527–1605, doi:10.1103/RevModPhys.84.1527. [Available at http://physics.nist.gov/cuu/Constants/.]
Murphy, T. W. (2013), Lunar laser ranging: the millimeter challenge, *Rep. Prog. Phys.*, *76*, 076901, doi:10.1088/0034-4885/76/7/076901.
Nakamura, Y. (1983), Seismic velocity structure of the lunar mantle, *J. Geophys. Res.*, *88*, 677–686, doi:10.1029/JB088IB01p00677.
Nakamura, Y. (2005), Far deep moonquakes and deep interior of the Moon, *J. Geophys. Res.*, *110*, E01001, doi:10.1029/2004JE002332.
Nakamura, Y., and J. Koyama (1982), Seismic *Q* of the lunar upper mantle, *J. Geophys. Res.*, *87*, 4855–4861, doi:10.1029/JB087IB06p04855.
Nakamura, Y., D. Lammlein, G. Latham, M. Ewing, J. Dorman, F. Press, and N. Toksöz (1973), New seismic data on the state of the deep lunar interior, *Science*, *181*, 49–51, doi:10.1126/science.181.4094.49.

Nakamura, Y., G. Latham, D. Lammlein, M. Ewing, F. Duennebier, and J. Dorman (1974), Deep lunar interior inferred from recent seismic data, *Geophys. Res. Lett.*, *1*, 137–140, doi:10.1029/GL001I003p00137.

Nakamura, Y., F. K. Duennebier, G. V. Latham, and H. J. Dorman (1976), Structure of the lunar mantle, *J. Geophys. Res.*, *81*, 4818–4824, doi:10.1029/JB081I026p04818.

Neumann, G. A. (2013), LRO Lunar Orbiter Laser Altimeter, PDS release of 15 March. [Available at http://imbrium.mit.edu/DATA/LOLA_SHADR/.]

Nimmo, F., U. H. Faul, and E. J. Garnero (2012), Dissipation at tidal and seismic frequencies in a melt-free Moon, *J. Geophys. Res.*, *117*, E09005, doi:10.1029/2012JE004160.

Park, R. S., S. W. Asmar, E. G. Fahnestock, A. S. Konopliv, W. Lu, and M. M. Watkins (2012), Gravity Recovery and Interior Laboratory simulations of static and temporal gravity field, *J. Spacecr. Rockets*, *49*, 390–400, doi:10.2514/1.A32117.

Peale, S. J. (1969), Generalized Cassini's laws, *Astron. J.*, *74*, 483–489, doi:10.1086/110825.

Petit, G., and B. Luzum (Eds.) (2010), *IERS Conventions (2010)*, *IERS Tech. Note 36*, 179 pp., Verlag des Bundesamts für Kartographie und Geodäsie, Frankfurt am Main. [Available at http://www.iers.org/TN36/].

Ping, J. S., Q. Huang, J. G. Yan, J. F. Cao, G. S. Tang, and R. Shu (2009), Lunar topographic model CLTM-s01 from Chang'E-1 laser altimeter, *Sci. China G*, *52*, 1105–1114, doi:10.1007/s11433-009-0144-8.

Rambaux, N., and J. G. Williams (2011), The Moon's physical librations and determination of their free modes, *Celest. Mech. Dyn. Astron.*, *109*, 85–100, doi:10.1007/s10569-010-9314-2.

Ries, J. C. (2007), Satellite laser ranging and the terrestrial reference frame; Principal sources of uncertainty in the determination of the scale, *Geophys. Res. Abstr.*, *9*, abstract 10809, EGU General Assembly, Vienna, Austria, 15–20 April.

Ries, J. C., R. J. Eanes, C. K. Shum, and M. M. Watkins (1992), Progress in the determination of the gravitational coefficient of the Earth, *Geophys. Res. Lett.*, *19*, 529–531, doi:10.1029/92GL00259.

Roncoli, R. B., and K. K. Fujii (2010), Mission design overview for the Gravity Recovery and Interior Laboratory (GRAIL) mission, in *AIAA/AAS Astrodynamics Specialist Conference*, Paper AIAA 2010-8383, 2010 AIAA Meeting Papers on Disc, vol. 15(9), AIAA, Washington, D. C., doi:10.2514/6.2010-8383. [Available at http://arc.aiaa.org/doi/abs/10.2514/6.2010-8383.]

Russell, C. T., P. J. Coleman Jr., and B. E. Goldstein (1981), Measurements of the lunar induced magnetic moment in the geomagnetic tail: Evidence for a lunar core?, *Proc. Lunar Planet. Sci. Conf.*, *12th*, pp. 831–836, Pergamon Press, New York and Oxford.

Sanloup, C., F. Guyot, P. Gillet, G. Fiquet, M. Mezouar, and I. Martinez (2000), Density measurements of liquid Fe-S alloys at high pressure, *Geophys. Res. Lett.*, *27*, 811–814, doi:10.1029/1999GL008431.

Sanloup, C., F. Guyot, P. Gillet, and Y. Fei (2002), Physical properties of liquid Fe alloys at high pressure and their bearings on the nature of metallic planetary cores, *J. Geophys. Res.*, *107*, 2272, doi:10.1029/2001JB000808.

Shea, E. K., B. P. Weiss, W. S. Cassata, D. L. Shuster, S. M. Tikoo, J. Gattacceca, T. L. Grove, and M. D. Fuller (2012), A long-lived lunar core dynamo, *Science*, *335*, 453–456, doi:10.1126/science.1215359.

Shimizu, H., M. Matsushima, F. Takahashi, H. Shibuya, and H. Tsunakawa (2013), Constraint on the lunar core size from electromagnetic sounding based on magnetic field observations by an orbiting satellite, *Icarus*, *222*, 32–43, doi:10.1016/j.icarus.2012.10.029.

Smith, D. E., M. T. Zuber, G. A. Neumann, and F. G. Lemoine (1997), Topography of the Moon from the Clementine lidar, *J. Geophys. Res.*, *102*, 1591–1611, doi:10.1029/96JE02940.

Smith, D. E., et al. (2010), Initial observations from the Lunar Orbiter Laser Altimeter (LOLA), *Geophys. Res. Lett.*, *37*, L18204, doi:10.1029/2010GL043751.

Spohn, T., W. Konrad, D. Breuer, and R. Ziethe (2001), The longevity of lunar volcanism: Implications of thermal evolution calculations with 2D and 3D mantle convection models, *Icarus*, *149*, 54–65.

Standish, E. M., and J. G. Williams (2012), Orbital ephemerides of the Sun, Moon, and planets, in *Explanatory Supplement to the Astronomical Almanac*, 3rd ed., edited by S. Urban and P. K. Seidelmann, pp. 305–345, Univ. Science Books, Mill Valley, Calif. [Available at http://iau-comm4.jpl.nasa.gov/XSChap8.pdf.]

Stevenson, D. J., and C. F. Yoder (1981), A fluid outer core for the Moon and its implications for lunar dissipation, free librations, and magnetism, *Lunar Planet. Sci.*, *12*, 1043–1045.

Suavet, C., B. P. Weiss, W. S. Cassata, D. L. Shuster, J. Gattacceca, L. Chan, I. Garrick-Bethell, J. W. Head, T. L. Grove, and M. D. Fuller (2013), Persistence and origin of the lunar core dynamo, *Proc. Natl. Acad. Sci. U.S.A.*, *110*, 8453–8458, doi:10.1073/pnas.1300341110.

Toksöz, M. N., A. M. Dainty, S. C. Solomon, and K. R. Anderson (1974), Structure of the Moon, *Rev. Geophys. Space Phys.*, *12*, 539–567, doi:10.1029/RG012I004p00539.

Usselman, T. M. (1975), Experimental approach to the state of the core: Part I. The liquidus relations of the Fe-rich portion of the Fe-Ni-S system from 30 to 100 kb, *Am. J. Sci.*, *275*, 278–290, doi:10.2475/ajs.275.3.278.

Wahr, J., and Z. Bergen (1986), The effects of mantle anelasticity on nutations, Earth tides, and tidal variations in rotation rate, *Geophys. J. R. Astron. Soc.*, *87*, 633–668, doi:10.1111/j.1365-246X.1986.tb06642.x.

Ward, W. R. (1975), Past orientation of the lunar spin axis, *Science*, *189*, 377–379, doi:10.1126/science.189.4200.377.

Weber, R. C., P.-Y. Lin, E. J. Garnero, Q. Williams, and P. Lognonne (2011), Seismic detection of the lunar core, *Science*, *331*, 309–312, doi:10.1126/science.1199375.

Wieczorek, M. A., and M. T. Zuber (2002), The "core" of the Moon: Iron or titanium rich?, *Lunar Planet. Sci.*, *33*, abstract 1384.

Wieczorek, M. A., et al. (2006), The constitution and structure of the lunar interior, in *New Views of the Moon*, Rev. Mineral. Geochem., vol. 60, edited by B. L. Jolliff et al., pp. 221–364, The Mineralogy Society of America, Chantilly, Va.

Wieczorek, M. A., et al. (2013), The crust of the Moon as seen by GRAIL, *Science*, *339*, 671–675, doi:10.1126/Science.1231530.

Williams, J. G. (2007), A scheme for lunar inner core detection, *Geophys. Res. Lett.*, *34*, L03202, doi:10.1029/2006GL028185.

Williams, J. G., M. A. Slade, D. H. Eckhardt, and W. M. Kaula (1973), Lunar physical librations and laser ranging, *Moon*, *8*, 469–483, doi:10.1007/BF00562071.

Williams, J. G., D. H. Boggs, C. F. Yoder, J. T. Ratcliff, and J. O. Dickey (2001), Lunar rotational dissipation in solid body and molten core, *J. Geophys. Res.*, *106*, 27,933–27,968, doi:10.1029/2000JE001396.

Williams, J. G., D. H. Boggs, and W. M. Folkner (2008), DE421 Lunar Orbit, Physical Librations, and Surface Coordinates, IOM 335-JW,DB,WF-20080314-001, Jet Propul. Lab., Pasadena, Calif., 14 March.

Williams, J. G., D. H. Boggs, and W. M. Folkner (2013), DE430 Lunar Orbit, Physical Librations, and Surface Coordinates, IOM 335-JW,DB,WF-20130722-016, Jet Propul. Lab., Pasadena, Calif., 22 July.

Williams, J. G., D. H. Boggs, and J. T. Ratcliff (2014), Free libration modes of a structured Moon, Abstract 1579 presented at Lunar and Planetary Science Conference, XLV, The Woodlands, TX, 17–21 March.

Zhong, S., C. Qin, G. A, and J. Wahr (2012), Can tidal tomography be used to unravel the long-wavelength structure of the lunar interior?, *Geophys. Res. Lett.*, *39*, L15201, doi:10.1029/2012GL052362.

Ziethe, R., K. Seiferlin, and H. Hiesinger (2009), Duration and extent of lunar volcanism: Comparison of 3D convection models to mare basalt ages, *Planet. Space Sci.*, *57*, 784–796, doi:10.1016/j.pss.2009.02.002.

Zuber, M. T., D. E. Smith, D. H. Lehman, T. L. Hoffman, S. W. Asmar, and M. M. Watkins (2013a), Gravity Recovery and Interior Laboratory (GRAIL): Mapping the lunar interior from crust to core, *Space Sci. Rev.*, *178*, 3–24, doi:10.1007/s11214-012-9952-7.

Zuber, M. T., et al. (2013b), Gravity field of the Moon from the Gravity Recovery and Interior Laboratory (GRAIL) mission, *Science*, *339*, 668–671, doi:10.1126/science.1231507.